Some New Lidar Equations for Laser Pulses Scattered Back from Optically Thick Media such as Clouds, Dense Aerosol Plumes, Sea Ice, Snow, and Turbid Coastal Waters

Anthony B. Davis

Jet Propulsion Laboratory, California Institute of Technology,
4800 Oak Grove Drive, Pasadena, CA 91109, USA

ABSTRACT

I survey the theoretical foundations of the slowly-but-surely emerging field of multiple scattering lidar, which has already found applications in atmospheric and cryospheric optics that I also discuss. In multiple scattering lidar, returned pulses are stretched far beyond recognition, and there is no longer a one-to-one connection between range and return-trip timing. Moreover, one can exploit the radial profile of the diffuse radiance field excited by the laser source that, by its very nature, is highly concentrated in space and collimated in direction. One needs, however, a new class of lidar equations to explore this new phenomenology. A very useful set is derived from radiative diffusion theory, which is found at the opposite asymptotic limit of radiative transfer theory than the conventional (single-scattering) limit used to derive the standard lidar equation. In particular, one can use it to show that, even if the simple time-of-flight-to-range connection is irretrievably lost, multiply-scattered lidar light can be used to restore a unique profiling capability with coarser resolution but much deeper penetration into a wide variety of optical thick media in nature. Several new applications are proposed, including a laser bathymetry technique that should work for highly turbid coastal waters.

Keywords: pulse stretching, multiple scattering, Green functions, clouds, aerosol plumes, sea ice, snow, laser bathymetry, turbid water

1. MOTIVATION & OUTLINE

Aerosol remote sensing techniques, both active and passive, fail for dense plumes near sources: fires, volcanoes, dust storms, etc. Indeed, the lidar's laser beam cannot penetrate the whole plume due to its shear opacity, and aerosol retrieval algorithms for processing passive observations are tuned for optically thinner horizontally uniform atmospheres. Yet these are important phenomena for air quality, aviation safety, weather and climate.

The base of boundary-layer stratus clouds, which matter tremendously for the radiation budget and even the hydrological cycle, can be so low that it is not detectable by a space-based millimeter radar due to insufficient vertical resolution, yet it is key to the atmosphere's thermodynamic profile, hence to global climate dynamics. Moreover, the smallest amount of drizzle swamps the mm-radar reflectivity, normally targeting droplets.

Sea ice thickness is a key property that is hard to determine by any means. Snow pack thickness is also a high-value target for water resource management. Even minute amounts of absorbing aerosol particulates in snow can radically change its albedo and lifecycle, and this also matters for the regional climate. Laser bathymetry has many operational applications, but it breaks down in highly turbid waters where the two-way transmitted pulse is all but extinguished by the opaque medium.

All of these remote sensing challenges have, at least in principle, a common solution: multiple scattering lidar, both ground- and space-based, or airborne.

In this report, I will survey the theoretical background as well as several field demonstrations and feasibility studies, published or not, that collectively show what kinds of opportunities open up when the conventional

Further author information:
E-mail: Anthony.B.Davis@jpl.nasa.gov, Telephone: 1 818 354 0450

lidar equation (based on a single back-scattering and two-way transmission) is abandoned in favor of multiple-scattering solutions of the full time-dependent 3D radiative transfer problem for pulsed laser sources, a.k.a. space-time Green functions of optical media. Closed-form expressions derived in the asymptotic limit of large scattering coefficients (radiative diffusion theory) are particularly useful for mining the highly-scattered returns for physical for information content. That form of analysis will be applied to the above-listed problems in remote sensing of the environment, and instrumental implementation challenges will be discussed.

The outline of this report is as follows. In the next Section, we put the standard "lidar equation" in the broader context of full-blown radiative transfer (RT) theory. In Section 3, we survey the theory of radiative diffusion in application to lidar; it is an approximation at the opposite end of the optical thickness scale than single scattering (hence the standard lidar equation). In Section 4, we visit a number of realized or proposed applications of multiple scattering lidar: clouds (§4.2), aerosol plumes (§4.3), snow and sea ice (§4.4), and bathymetry in highly turbid shallow waters (§4.5). Finally, we offer some parting remarks in Section 5.

2. LIDAR EQUATIONS IN THE FRAME OF RADIATIVE TRANSFER

2.1 Implicit Definition of the General (Multiple Scattering) Lidar Equation

The defining pulsed laser sources used in lidar technology are excellent physical approximations of every imaginable "delta" in photon state space. Indeed, drawing on their quantum-physical definition as eigenmodes of the quantized EM field, photons have energy, momentum and spin, which translate to wavelength, direction of propagation ($\mathbf{\Omega}$), and state of polarization. Interestingly, lasers bring one more Dirac δ to the table: they are, for all practical purposes, point-wise sources of light.* The upshot is that, if we accept radiative transfer (RT) theory as good enough for predicting signals based on atmospheric scattering, then lasers excite RT Green functions. Mishchenko[1] derived RT microphysically from EM theory and statistical optics, with an emphasis on conditions of validity, which are well verified in most of the natural optical media considered in the present study.

Let $G(t, \boldsymbol{x}, \mathbf{\Omega})$ be the Green function for time-dependent scalar† RT for a δ-source at time $t = 0$, position $\boldsymbol{x} = (0, 0, 0)^{\mathrm{T}}$ in 3D space (assumed to be a boundary point), and $\mathbf{\Omega} = \hat{\mathrm{z}}$ (the unit vector in the vertical z direction). It verifies the following t-dependent 3D RT equation (RTE):

$$\left[\left(\frac{1}{c}\frac{\partial}{\partial t} + \mathbf{\Omega}\cdot\nabla\right) + \sigma(\boldsymbol{x})\right] G = S(t, \boldsymbol{x}, \mathbf{\Omega}) + Q(t, \boldsymbol{x}, \mathbf{\Omega}), \tag{1}$$

where $\sigma(\boldsymbol{x})$ is the spatially varying extinction coefficient—one of backscattering lidar's most valued targets.

Physically, (1) balances sources on the right-hand side and sinks on the left for the *diffuse/scattered* radiant energy budget of a narrow light beam going through $\boldsymbol{x}$ in direction $\mathbf{\Omega}$ (geometric optics are assumed). The *direct/un-scattered* light will be accounted for in the source term $Q(t, \boldsymbol{x}, \mathbf{\Omega})$ for the diffuse light field.

The tally of sinks is short: advection out of a small volume of interest, $[c^{-1}\partial_t + \mathbf{\Omega}\cdot\nabla]G$, or depletion by extinction in the medium, $\sigma(\boldsymbol{x})G$. If that is all we had (right-hand side of (1) vanishes) then we can specify an initial condition,

$$G(t, \boldsymbol{x}, \mathbf{\Omega}) = E_0\delta(t)\delta((\boldsymbol{x} - \boldsymbol{x}_0) - \|\boldsymbol{x} - \boldsymbol{x}_0\|\mathbf{\Omega}_0)\delta(\mathbf{\Omega} - \mathbf{\Omega}_0), \tag{2}$$

expressing that a pulse of light leaves at time $t = 0$ into direction $\mathbf{\Omega}_0$ from a position $\boldsymbol{x}_0$ in a plane perpendicular to $\mathbf{\Omega}_0$. We then have an exponentially decaying localized pulse propagating downwind of $(\boldsymbol{x}, \mathbf{\Omega})_0$:

$$G(t, \boldsymbol{x}, \mathbf{\Omega}) = E_0\delta(t - \ell/c)\delta((\boldsymbol{x} - \boldsymbol{x}_0) - \|\boldsymbol{x} - \boldsymbol{x}_0\|\mathbf{\Omega}_0)\delta(\mathbf{\Omega} - \mathbf{\Omega}_0)\exp\left(-\tau(\boldsymbol{x}_0; \boldsymbol{x})\right) \tag{3}$$

*In exact EM wave theory, as well as in hardware of course, this can only be approximated as a superposition of plane waves compatible with the prevailing diffraction phenomena.

†The more exact "vector" or polarized RT theory, where G would be a Stokes vector, is out of the present scope, and would not bring much more accuracy for the highly scattered, hence depolarized, signals of interest.

for $\ell\,(=\|\boldsymbol{x}-\boldsymbol{x}_0\|=ct)\geq 0$, and where

$$\tau(\boldsymbol{x}_0;\boldsymbol{x})=\int_0^{\|\boldsymbol{x}-\boldsymbol{x}_0\|}\sigma\left(\boldsymbol{x}_0+\frac{\boldsymbol{x}-\boldsymbol{x}_0}{\|\boldsymbol{x}-\boldsymbol{x}_0\|}\ell\right)\mathrm{d}\ell \tag{4}$$

is the optical distance between two points in the 3D medium.

Functions $S(t,\boldsymbol{x},\boldsymbol{\Omega})$ and $Q(t,\boldsymbol{x},\boldsymbol{\Omega})$ represent respectively the in-scattering of diffuse light, and our special choice of source for the Green function problem. For this scenario, we have

$$Q(t,\boldsymbol{x},\boldsymbol{\Omega})=E_\mathrm{c}\delta(t-z/c)\delta(\vec{\rho})\sigma_\mathrm{s}(\vec{0},z)p(\vec{0},z,\hat{z}\cdot\boldsymbol{\Omega})\exp\Big(-\tau(\vec{0},0;\vec{0},z)\Big) \tag{5}$$

where E_c is the total energy in the pulse, $\vec{\rho}=(x,y)^\mathrm{T}$ is the horizontal projection of $\boldsymbol{x}=(\vec{\rho},z)^\mathrm{T}$, $\sigma_\mathrm{s}(\boldsymbol{x})$ is the scattering coefficient, and $p(\boldsymbol{x},\boldsymbol{\Omega}'\cdot\boldsymbol{\Omega})$ in 1/sr is the phase function for scattering of light out of direction $\boldsymbol{\Omega}'$ and into $\boldsymbol{\Omega}$, both σ_s and p potentially vary in space. The exponential term is Beer's law for propagating the pulse vertically from the origin $\boldsymbol{x}=(\vec{0},0)^\mathrm{T}$ to $(\vec{0},z)^\mathrm{T}$. The (multiple) scattering source function however depends on the unknown quantity, $G(t,\boldsymbol{x},\boldsymbol{\Omega})$, and is always given by

$$S(t,\boldsymbol{x},\boldsymbol{\Omega})=\sigma_\mathrm{s}(\boldsymbol{x})\int_{4\pi}p(\boldsymbol{x},\boldsymbol{\Omega}'\cdot\boldsymbol{\Omega})G(t,\boldsymbol{x},\boldsymbol{\Omega}')\mathrm{d}\boldsymbol{\Omega}'. \tag{6}$$

For future use,

$$\varpi_0(\boldsymbol{x})=\sigma_\mathrm{s}(\boldsymbol{x})/\sigma(\boldsymbol{x}) \tag{7}$$

is the single scattering albedo (SSA), the probability between 0 and unity for the light-matter interaction to end in scattering rather than absorption; by the same token, $\sigma_\mathrm{a}(\boldsymbol{x})=\sigma(\boldsymbol{x})-\sigma_\mathrm{s}(\boldsymbol{x})$ is the absorption coefficient.

This RT problem still needs boundary conditions (BCs) at the top and bottom of the horizontal plane-parallel slab $0\leq z\leq H$. In short, we need to specify spatially and angularly the incoming radiation at those two planes.

We will assume that the $z=H$ boundary (opposite the origin of the laser source) can be partially reflective, for simplicity, in a spatially uniform and directionally Lambertian (isotropic) fashion with an albedo $\alpha\geq 0$. Moreover, for reasons clarified further on, there is the possibility of a pulsed point-source of isotropically diffuse light with total energy $E_\mathrm{d}\geq 0$ at $z=0$ and $\vec{\rho}=\vec{0}$, i.e., collocated with the impact point of the laser beam modeled in the bulk source term $Q(t,\vec{\rho},z,\boldsymbol{\Omega})$ in (5). In other words,

$$G(t,\vec{\rho},0,\boldsymbol{\Omega})=\frac{E_\mathrm{d}}{\pi}\,\delta(t)\delta(\vec{\rho}) \tag{8}$$

for $\Omega_z>0$, and

$$G(t,\vec{\rho},H,\boldsymbol{\Omega})=\frac{\alpha}{\pi}\,F_z^{(+)}(t,\vec{\rho},H) \tag{9}$$

for $\Omega_z<0$. We have introduced here instantaneous hemispherical radiative fluxes for light crossing a plane with normal $\hat{\mathrm{n}}$ in one direction or the other at space-time position $(t,\boldsymbol{x})$:

$$F_{\hat{\mathrm{n}}}^{(\pm)}(t,\boldsymbol{x})=\int_{\pm\hat{\mathrm{n}}\cdot\boldsymbol{\Omega}>0}G(t,\boldsymbol{x},\boldsymbol{\Omega})|\hat{\mathrm{n}}\cdot\boldsymbol{\Omega}|\mathrm{d}\boldsymbol{\Omega}. \tag{10}$$

This completes the description of the theoretical and computational RT problem for the Green function associated with a boundary source, either well-collimated ($E_\mathrm{c}=1,E_\mathrm{d}=0$) or diffuse ($E_\mathrm{c}=0,E_\mathrm{d}=1$), which can be assumed unitary without loss of generality. Note that, if we shut down $Q(t,\boldsymbol{x},\boldsymbol{\Omega})$ in (1) by setting $E_\mathrm{c}=0$ in (5), all the light is diffuse: there is no longer any well-collimated light emanating from a laser-type source. That changes somewhat the meaning of $G(t,\boldsymbol{x},\boldsymbol{\Omega})$, which now contains light *directly* transmitted from the diffuse point source. Conversely, if $E_\mathrm{c}>0$, then $G(t,\boldsymbol{x},\boldsymbol{\Omega})$ contains all the diffuse light whether scattering once or more,

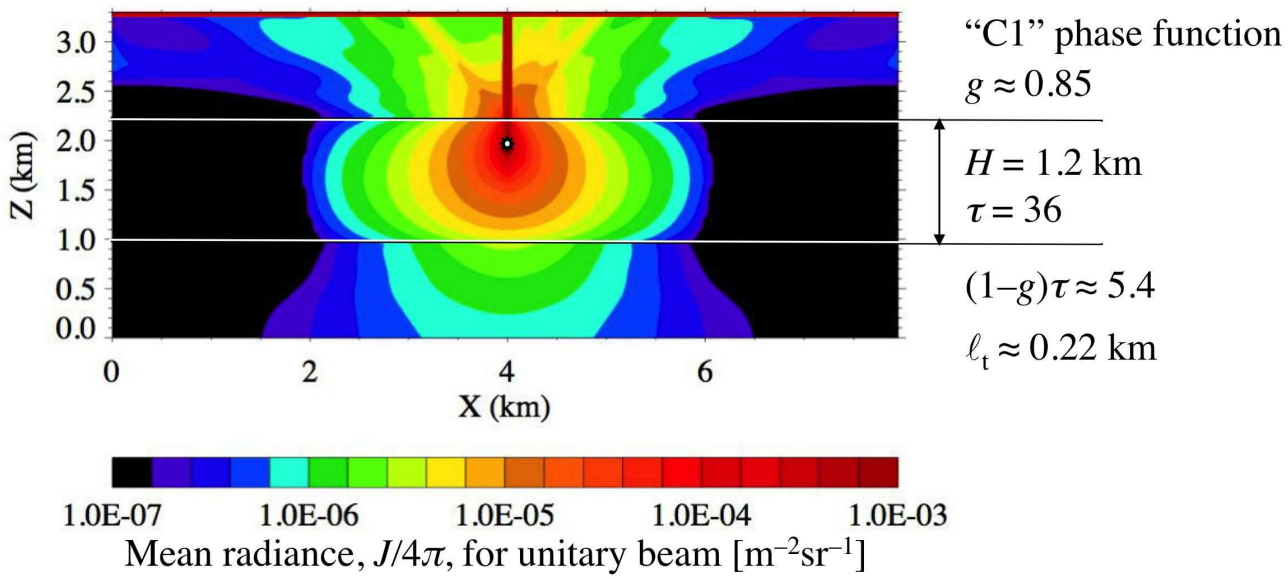

Figure 1. Mean radiance for the steady-state "searchlight" problem in a finite homogeneous slab. Note the deep penetration of the laser light into this cloud with an optical depth $\tau = 36$ in the absence of absorption by water droplets, as is the case for (say) 532 nm laser light. The small black and white symbol is discussed in §4.1. The basis of this plot was graciously contributed by Dr. K. Franklin Evans (U. of Colorado).

or coming directly from a diffuse source while light coming directly from the collimated source is contained in $Q(t, \boldsymbol{x}, \boldsymbol{\Omega})$.

That said, the above 3D RT problem with at once a non-uniform source and spatially varying optical properties only has numerical solutions. Some less general problems in uniform media may be amenable to analytical methods, e.g., steady-state pencil-beam, isotropic scattering, semi-infinite media, etc.[2–5]

Figure 1 illustrates a numerical solution of the steady-state (i.e., cw laser source) version of the general time-dependent RT problem defined in the above. It was solved with the Spherical Harmonic - Discrete Ordinate Method (SHDOM)[6] for a uniform non-absorbing ($\varpi_0 = 1$) cloud of thickness $H = 1.2$ km with uniform extinction $\sigma = 30$ km^{-1}, hence an optical thickness $\tau = \sigma H = 36$. The phase function is for a "C1" distribution of droplet sizes[7] in a Mie scattering computation[8] for $\lambda = 532$ nm (i.e., 2×Nd:YAG source). Mean radiance, $J/4\pi$ from (25) below, is plotted for a domain larger than the cloud itself. The "rays" emanating from the source region near the top of the cloud are an artifact of the discrete ordinates scheme (in this case, using $N_\mu = 12$ and $N_\phi = 24$).

In lidar observations, with all orders of scattering included, the field of primary interest is the light escaping the optical medium through the same ($z = 0$) boundary as where the laser pulse is injected, i.e., $G(t, \vec{\rho}, 0, \boldsymbol{\Omega})$ with $t \geq 0$, $\rho \geq 0$ and $\Omega_z < 0$.

2.2 Remote Sensing with Multiple Scattering Lidar: Clouds and Beyond

Imagine, for instance, a sensor at a large standoff distance with a relatively large field-of-view (FOV). Given the high degree of collimation of laser light, this could be a monostatic system, and was indeed realized in 1994 with the Space Shuttle during the Lidar-In-space Technology Experiment (LITE).[9‡] Such a system measures the spatially-integrated Green function for radiance escaping orthogonally as a function of time:

$$I(t) = \int_0^\infty G(t, \vec{\rho}, 0, -\hat{z}) \mathrm{d}\vec{\rho}. \tag{11}$$

‡Spaceborne lidars since then have more focused beams and much narrower FOVs.

This time-varying signal is one of many possible *multiple scattering* lidar equations defined implicitly through $G(t, \vec{\rho}, 0, -\hat{z})$ by the integro-differential equation set up in (1)–(6) subject to BCs in (8)–(9) with $\alpha = 0$ in the case of LITE probing an opaque spatially variable marine stratocumulus layer. This is a computational challenge even for media with (assumed) uniform optical properties.

Another example is the ground-based Wide-Angle Imaging Lidar (WAIL).[10] Its signal can be modeled by $G(t, \vec{\rho}, z_{\rm cloud}, \mathbf{\Omega}(\vec{\rho}))$ where $z_{\rm cloud}$ is the range to cloud *base* and $\vec{\rho}$ scans all the pixels of the temporal sequence of images ("movie") formed at its focal plane, controlling the escape direction $\mathbf{\Omega}(\vec{\rho})$ in the process. For WAIL's airborne counterpart, the cloud THickness from Off-beam Returns (THOR) system[11] and the ground-based system using Multiple FOVs (MFOV) technology[12,13] measure the same sample of the Green function (except for $z_{\rm cloud}$ now being range to cloud *top* in the THOR configuration) but rewritten as $G(t, \vec{\rho}(\mathbf{\Omega}), z_{\rm cloud}, \mathbf{\Omega})$ where the viewing direction now controls the horizontal coordinate. However, rather than form an image like WAIL, THOR and MFOV instrumentally perform broad integrals over all azimuthal angles ϕ and different bands of nadir angles θ in $\mathbf{\Omega}(\theta, \phi)$ resulting in as many time-dependent signals as there are intervals for θ.[§] More details on WAIL, THOR and other systems will be provided in §4.

Table 1 summarizes the main parameters that have been introduced in either an RTE or a BC along with their appropriate ranges. In anticipation of Section 4, we also mark them as primary or secondary remote sensing targets dependent on the medium being probed.

Table 1. The 4 main parameters in new lidar equations are displayed in terms of the 6 cases we investigate in Section 4. One "?" marks a remote sensing unknown of primary interest; two "??" marks one of secondary interest.

Parameter:	single scattering albedo	optical thickness	geometric thickness	surface albedo
Symbol:	ϖ_0	$\tau = \sigma H$	H	α
Stratiform clouds	1	$? \gg 1$	$? < \infty$	0
Aerosol plumes	$? \lesssim 1$	$? \gg 1$	$? < \infty$	0
Sea ice or clean snow	1	$?? \gg 1$	$? < \infty$	0
Dirty snow	$? \lesssim 1$	∞	∞	n/a
Bathymetry & turbidity	$?? \lesssim 1$	$?? \gg 1$	$? < \infty$	$?? > 0$

2.3 Explicit Expression for the Standard (Single Scattering) Lidar Equation

In conventional backscattering lidar, the source function $S(t, \boldsymbol{x}, \mathbf{\Omega})$ in (6) that describes how *diffuse* laser light is scattered back into the beam of interest is neglected. In other words, we are only interested in the contribution to $G(t, \vec{\rho}, 0, \mathbf{\Omega})$ from single scattering. However, a look at $S(t, \boldsymbol{x}, \mathbf{\Omega})$ in (6) shows that it cannot be "turned off" except by setting $\sigma_{\rm s} = 0$, but that also kills the key source term $Q(t, \boldsymbol{x}, \mathbf{\Omega})$ in (5). In other words, once the scattering is started, it cannot be stopped and will generate a systematic forward model error in lidar retrievals. The only question is: How to keep $S \ll Q$? And the only answer is to stay away from even moderate optical depth in (4). Although the exponential function it drives in the RTE decays rapidly, that only means that a $2^{\rm nd}$ scattering will happen sooner, then a $3^{\rm rd}$ and so on.

The radical choice to neglect S however makes the above problem analytically tractable. Thus, we can derive the standard lidar equation (in monostatic configuration) simply by estimating the time dependent radiance at the source position but propagating in the opposite direction. For a ground-based lidar ($H \to \infty$), this is

[§]The key difference between THOR, a cloud-only instrument, and MFOV systems, which apply to aerosols as well as clouds, is the much larger outer limit of θ for THOR which naturally leads to different kinds of forward model and retrieval scheme.

expressed (without the usual "R^2" term multiplying the left-hand side) as

$$\begin{aligned} G(t,\vec{\rho},0,-\hat{z}) &= \delta(\vec{\rho})\int_0^H \exp\left(-\tau(\vec{0},0;\vec{0},z)\right) Q(t-z/c,\vec{0},z,-\hat{z})\mathrm{d}z \\ &= E_\mathrm{c}\delta(\vec{\rho})\sigma_\mathrm{s}(\vec{0},z)p(\vec{0},z,-1)\exp(-2\tau(\vec{0},0;\vec{0},z))\Big|_{z=ct/2}. \end{aligned} \tag{12}$$

We recognize here the range $ct/2$ from the transmitter to where the optical "echo" originates. We also identify the important lidar backscatter function $\sigma_\mathrm{s}(\boldsymbol{x})p(\boldsymbol{x},-1)$, that can be separated from extinction $\sigma(\boldsymbol{x})$ only by choosing a value for the notorious "lidar ratio" $\varpi_0(\boldsymbol{x})p(\boldsymbol{x},-1)$ in 1/sr. Given this lidar ratio, typically as a constant, and the time-dependent signal on the left-hand side of (12), one can derive the extinction profile $\sigma(\vec{0},z)$ above the lidar system using, e.g., the Klett algorithm.[14]

For a downward-looking airborne or space-based lidar (finite H), we need to add to the above the (assumed) Lambertian surface term for a single reflection. For that term, we turn to (9) and (10), which yields $F_z^{(+)}(t,\vec{0},H) = E_\mathrm{c}\delta(t-H/c)\delta(\vec{0})\exp(-\tau(\vec{0},0;\vec{0},H))$. Factoring the return trip of the pulse through the whole medium, we find

$$\begin{aligned} G(t,\vec{\rho},0,-\hat{z}) &= E_\mathrm{c}\delta(\vec{\rho})\left[\sigma_\mathrm{s}(\vec{0},\frac{ct}{2})p(\vec{0},\frac{ct}{2},-1)\exp(-2\tau(\vec{0},0;\vec{0},\frac{ct}{2}))\right. \\ &+ \left.\frac{\alpha}{\pi}\exp(-2\tau(\vec{0},0;\vec{0},H))\delta\left(t-\frac{2H}{c}\right)\right] \end{aligned} \tag{13}$$

We note that this contribution to the time-varying signal is, as expected, a spike at range $ct/2 = H$.

On physical grounds, multiple scattering is inevitable. There have therefore been many studies about how to correct for its impact on (12). These investigations rely on numerical solutions[15,16] of the general lidar equation defined implicitly in §2.1 or analytical approximations thereof.[17]

2.4 Laplace Transform of General Lidar RTE

Equation (11) is an instance where only the temporal aspect of the Green function is retained. Consider

$$\mathrm{d}\Pr(L)/\mathrm{d}L = \frac{I(L/c)}{c}\Big/\int_0^\infty I(t)\mathrm{d}t\ , \tag{14}$$

which can be interpreted as a probability density function (PDF) for the random pathlength $L = ct$ followed by the light in the multiple scattering medium (with $1/c$ being the Jacobian $|\partial t/\partial L|$). It can be used, for instance, to evaluate pathlength moments

$$\langle (ct)^q\rangle_I = \int_0^\infty (ct)^q\,\mathrm{d}\Pr(ct) \tag{15}$$

predicated, in this case, on normally escaping intensity.

Moments of a PDF supported by non-negative reals are easily computed by successive derivatives if one knows the characteristic (a.k.a. moment-generating) function

$$\langle \exp(-s'ct)\rangle_I = \int_0^\infty \exp(-s'ct)\mathrm{d}\Pr(ct). \tag{16}$$

which is easily obtained from the Laplace transform of $I(t)$ in (14):

$$\hat{I}(s) = \int_0^\infty \exp(-st)I(t)\mathrm{d}t, \tag{17}$$

using $s' = s/c$. The characteristic function method for moment estimation yields

$$\langle (ct)^q \rangle_I = \left(-\frac{\mathrm{d}}{\mathrm{d}s'} \right)^q \langle \exp(-s'ct) \rangle_I \Big|_{s=0} = \frac{1}{\hat{I}(0)} \left(-c\frac{\mathrm{d}}{\mathrm{d}s} \right)^q \hat{I}(s) \Big|_{s=0}. \tag{18}$$

In this study, we will use extensively the variability metric based on the ratio of the root-mean-square (RMS) over the mean, i.e., $\sqrt{\langle (ct)^2 \rangle}/\langle ct \rangle$. In the present case, using radiance I, this ratio is the square root of

$$\frac{\langle (ct)^2 \rangle_I}{\langle ct \rangle_I^2} = \hat{I}(0) \frac{\mathrm{d}}{\mathrm{d}s} \left(\frac{1}{\mathrm{d}\hat{I}/\mathrm{d}s} \right) \Big|_{s=0}. \tag{19}$$

As it turns out, $\hat{I}(s)$ and, more generally speaking, $\hat{G}(s', \boldsymbol{x}, \boldsymbol{\Omega})$ is in fact the solution of a more easily solved *steady-state* RTE obtained by taking the Laplace transform of both sides of (1), supplemented with transforms of (5)–(6). Assuming a uniform optical medium for simplicity, this results in

$$\left[\boldsymbol{\Omega} \cdot \nabla + (\sigma + s') \right] \hat{G} = \hat{S}(s', \boldsymbol{x}, \boldsymbol{\Omega}) + \hat{Q}(s', \boldsymbol{x}, \boldsymbol{\Omega}), \tag{20}$$

with

$$\hat{S}(s', \boldsymbol{x}, \boldsymbol{\Omega}) = \sigma_\mathrm{s} \int_{4\pi} p(\boldsymbol{\Omega}' \cdot \boldsymbol{\Omega}) \hat{G}(s', \boldsymbol{x}, \boldsymbol{\Omega}') \mathrm{d}\boldsymbol{\Omega}', \tag{21}$$

and

$$\hat{Q}(s', \boldsymbol{x}, \boldsymbol{\Omega}) = E_\mathrm{c} \delta(\vec{\rho}) \sigma_\mathrm{s} p(\hat{z} \cdot \boldsymbol{\Omega}) \exp\left(-(\sigma + s')z \right). \tag{22}$$

For BCs, we find

$$\hat{G}(s', \vec{\rho}, 0, \boldsymbol{\Omega}) = \frac{E_\mathrm{d}}{\pi} \delta(\vec{\rho}) \text{ for } \Omega_z > 0, \tag{23}$$

$$\hat{G}(s', \vec{\rho}, H, \boldsymbol{\Omega}) = \frac{\alpha}{\pi} \hat{F}_z^{(+)}(s', \vec{\rho}, H) \text{ for } \Omega_z < 0. \tag{24}$$

If, moreover, we consider only spatially integrated quantities, such as in (14), then the $\delta(\vec{\rho})$ terms can be removed from all the above, accordingly replace pulse energies $E_\mathrm{c,d}$ in J with steady flux densities $F_\mathrm{c,d}$ in W/m^2, and replace $\boldsymbol{x}$ or $(\vec{\rho}, z)$ with just z. This reduces the temporal Green function problem to a classic 1D RTE problem.

In other words, we have simply added $s' = s/c$ to the absorption coefficient σ_a in extinction σ's decomposition into $\sigma_\mathrm{s} + \sigma_\mathrm{a}$. even if $\sigma_\mathrm{a} = 0$, there is now an "effective" absorption coefficient. To underscore this formal equivalence between time-dependence and absorption, the key definition in (17) is sometimes called the "equivalence theorem".[18,19] From this standpoint, $I(L/c)/c$ is the given pathlength-dependent radiance observed in the absence of uniformly distributed (hence gaseous in the atmosphere) absorbing material, and $\hat{I}(s)$ is the computed radiance for a given absorption coefficient s/c.

It is noteworthy that not only are there many excellent numerical codes for solving the spatially-integrated version of (20)–(22) with BCs (23)–(24), there is an emerging observational technology where $\hat{I}(s', \boldsymbol{\Omega})$ is measured directly over a broad range of its argument. In this case, s' is the known absorption coefficient of a uniform gas. This technology is *passive* and uses the sun as a plentiful source: oxygen A- or B-band spectroscopy (at as high a resolution and out-of-band rejection as possible[20]). If we know $\hat{I}(s', \boldsymbol{\Omega})$, then we can easily compute the sequence of temporal (equivalently, pathlength) moments in (18). Anything we can learn about the medium from them can thus be inferred from this interesting passive modality.

Further discussion of high-resolution O_2 spectroscopy is out of the scope of this report. We refer to Davis et al.[21] for more details in a formalism with unified signal physics between the passive and active approaches. We simply note the natural complementarity of the two approaches with shared signal models in spite of radically different hardware. Indeed, multiple scattering lidar signals are weak and, so far, observed only by night. The solar background is likely to swamp them unless very sophisticated filtering is brought to bear.[22] But sunrise is precisely when the passive A-band spectroscopy becomes available.

3. LIDAR EQUATIONS IN THE FRAME OF DIFFUSION THEORY

Here, we introduce formally the radiative diffusion approximation that is as useful for highly opaque media as the single scattering approximation is for optically thin ones.

3.1 The Hierarchy of Transport Equations for Angular Moments

Define the three first directional momenta of the Green function:

$$J(ct, \boldsymbol{x}) = \int_{4\pi} G(ct, \boldsymbol{x}, \boldsymbol{\Omega}) \mathrm{d}\boldsymbol{\Omega}; \tag{25}$$

$$\boldsymbol{F}(ct, \boldsymbol{x}) = \int_{4\pi} \boldsymbol{\Omega} G(ct, \boldsymbol{x}, \boldsymbol{\Omega}) \mathrm{d}\boldsymbol{\Omega}; \tag{26}$$

$$\mathsf{K}(ct, \boldsymbol{x}) = \int_{4\pi} \boldsymbol{\Omega}\boldsymbol{\Omega} G(ct, \boldsymbol{x}, \boldsymbol{\Omega}) \mathrm{d}\boldsymbol{\Omega}. \tag{27}$$

Their Laplace transforms, $[J, \boldsymbol{F}, \mathsf{K}](s, \boldsymbol{x})$, are defined similarly where, from now on, we use s instead of s' as the Laplace conjugate variable for pathlength ct. Also, we will no longer use the "circumflex" notation to distinguish a quantity from its Laplace transform since it will be clear from context.

Physically, J in (25) has units of flux [W/m^2] but is a measure of radiant energy density in space-time, irrespective of direction of propagation. In fact, this *scalar* flux can be linked to radiant energy density U in J/m^3: $U = J/c$. By the same token, *vector* flux $\boldsymbol{F}$ measures the mean "current" of the flow of radiant energy. using the definitions in (10), one can show that the net radiative flux across a plane normal to $\hat{\mathrm{n}}$ at any $(ct, \boldsymbol{x})$ is

$$\hat{\mathrm{n}} \cdot \boldsymbol{F} = F_{\hat{\mathrm{n}}}^{(+)} - F_{\hat{\mathrm{n}}}^{(-)} \tag{28}$$

Finally, the *tensor* flux K captures the pressure and stress in the radiant energy flow.

Recall that we've assumed the the scattering phase function depends only on the scattering angle $\theta_\mathrm{s} = \cos^{-1}(\boldsymbol{\Omega} \cdot \boldsymbol{\Omega}')$. Our normalization convention is

$$\int_{4\pi} p(\boldsymbol{\Omega} \cdot \boldsymbol{\Omega}') \mathrm{d}\boldsymbol{\Omega}' = 1, \tag{29}$$

and we define the "asymmetry factor" of the phase function as

$$g = \int_{4\pi} \boldsymbol{\Omega} \cdot \boldsymbol{\Omega}' p(\boldsymbol{\Omega} \cdot \boldsymbol{\Omega}') \mathrm{d}\boldsymbol{\Omega}', \tag{30}$$

which is a simple measure of how forward-peaked is the phase function. For liquid water clouds, $g \approx 0.85$.

Taking the first two directional integrals of all the terms in the steady-state 1D RTE (20)–(22), we find

$$\nabla \cdot \boldsymbol{F} = -(\sigma_\mathrm{a} + s) J + E_\mathrm{c} \sigma_\mathrm{s} \delta(\vec{\rho}) \exp(-(\sigma + s) z), \tag{31}$$

$$\nabla \cdot \mathsf{K} = -(\sigma_\mathrm{t} + s) \boldsymbol{F} + E_\mathrm{c} g \sigma_\mathrm{s} \delta(\vec{\rho}) \exp(-(\sigma + s) z), \tag{32}$$

where

$$\sigma_\mathrm{t} = (1 - \varpi_0 g)\sigma = (1 - g)\sigma_\mathrm{s} + \sigma_\mathrm{a}, \tag{33}$$

is the "transport" extinction coefficient.

Recall that, at least in uniform optical media, $\ell = 1/\sigma$ is the characteristic lengthscale in Beer's law of light propagation subject to an exponential decay in the source-free RT problem solved with (3). It is often called the "photon mean-free-path" (MFP) by analogy with the kinetic theory of gases. However, since phase functions of atmospheric and hydrospheric particulates are often very forward-peaked, a scattering every ℓ on average does

generally not translate into a major change in direction. That is what the "scaled" or transport MFP $\ell_\mathrm{t} = 1/\sigma_\mathrm{t}$ is about. It is $1/(1-\varpi_0 g)\times$ longer than ℓ ($\approx$6.7$\times$ in clouds) but, by that many scatterings, directional memory is lost. We might as well wait that much longer, and then scatter isotopically.

The angularly-integrated radiation transport equations in (31)–(32) are the beginning of an infinite sequence calling for ever higher counterparts of the three quantities in (25)–(27). The first, (31) expresses locally the conservation of radiant energy while the second (32) expresses locally the conservation of momentum in the light field. In both cases, the contributions of diffuse (terms with $J, \boldsymbol{F}$, or K) and non-scattered (last terms) light are clearly separated when $E_\mathrm{c} > 0$ and $E_\mathrm{d} = 0$.

3.2 The Eddington Closure

The diffusion approximation follows immediately from the Eddington closure for the above hierarchy of exact space-time transport equations:

$$\mathsf{K}(s, \boldsymbol{x}) \equiv \frac{J(s, \boldsymbol{x})}{3}\mathbf{1}, \tag{34}$$

where $\mathbf{1}$ denotes the unity diagonal tensor. This is tantamount to stating that radiation pressure is isotropic, thus expressing that the radiation field is "thermalized" by the optical medium.

The RT problem at hand has thus become a coupled pair of PDEs starting with the (exact) energy conservation law in (31), and ending with the constitutive relation

$$\nabla J/3 = -(\sigma_\mathrm{t} + \zeta s)\boldsymbol{F} + E_\mathrm{c} g \sigma_\mathrm{s} \delta(\vec{\rho}) \exp(-(\sigma + s)z), \tag{35}$$

where we set $\zeta = 1$ at present. If $E_\mathrm{c} = 0$ (only diffuse boundary sources are present), then we retrieve Fick's law, $\boldsymbol{F} = -D\nabla J$, where $D = 1/(3(\sigma_\mathrm{t} + s))$ is the radiative diffusivity constant.[¶]

Now, technically speaking, the coupled PDEs in the time-domain leading to (31) and (35) in Laplace space, do not amount to a diffusion model per se but to the slightly superior "telegrapher's problem." The only difference is the first occurrence of "s" on the right-hand side of (35): it comes from $\partial_{ct}\boldsymbol{F}$, which is explicitly neglected in classic diffusion theory.[‖] In the present setting, we can back off to classic diffusion be setting $\zeta = 0$.

Eddington's closure has a major impact on $G(ct, \boldsymbol{x}, \boldsymbol{\Omega})$ in (25)–(27). Specifically, it is exactly as if the radiance field was reduced to a 1st-order expansion in spherical harmonics:

$$G(ct, \boldsymbol{x}, \boldsymbol{\Omega}) = \frac{1}{4\pi}\left[J(ct, \boldsymbol{x}) + 3\boldsymbol{\Omega}\cdot\boldsymbol{F}(ct, \boldsymbol{x})\right], \tag{36}$$

and similarly for $G(s, \boldsymbol{x}, \boldsymbol{\Omega})$ with $J(s, \boldsymbol{x})$ and $\boldsymbol{F}(s, \boldsymbol{x})$. Consequently, the only spherical harmonics of the phase function that matter here are the 0th- and 1st-order terms:

$$p(\boldsymbol{\Omega}\cdot\boldsymbol{\Omega}') = \frac{1}{4\pi}\left[1 + 3g\boldsymbol{\Omega}\cdot\boldsymbol{\Omega}'\right]. \tag{37}$$

Note that to keep the scalar flux and phase function non-negative, we should require $\|\boldsymbol{F}\| \leq J/3$ and $g \leq 1/3$. But that is not always possible in natural media. We must therefore be vigilent about non-physical predictions by diffusion theory, which doesn't mean that the general trends it predicts aren't correct.

Physically, (36) means that in direction space the radiance field is everywhere and at all times made of a monopole (isotropic term) superposed with a dipole: radiance traces a sine function in angle in every plane; its amplitude is maximal when the plane contains $\boldsymbol{F}$, and it vanishes in the plane perpendicular to $\boldsymbol{F}$. This is a reasonable assumption deep enough inside opaque media such as clouds, and has indeed been observed directly

[¶] In particle diffusion (a.k.a. Brownian motion) theory, diffusivity is defined as the proportionality constant in Fick's law, $\boldsymbol{j} = -D\nabla n$, where $\boldsymbol{j}$ is particle current density in $[\mathrm{s}^{-1}\mathrm{m}^{-2}]$ is analogous to our vector flux $\boldsymbol{F}$, and particle density n in $[\mathrm{m}^{-3}]$ is analogous to our radiant energy density $U = J/c$. Thus, the classic expression for diffusivity $D = c\ell_\mathrm{t}/3$ in $[\mathrm{m}^2/\mathrm{s}]$ is retrieved.

[‖] This is the origin of the violations of causality that strict diffusion theoretical solutions show at very early times, with ρ increasing as $\sqrt{t}$. The telegrapher's equation does not have this issue.

inside clouds when expected.[23,24] Equation (36) is at its best if we are only concerned with the diffuse light field, i.e., we use the representation of laser sources where $E_c > 0$ and $E_d = 0$. In that case, the highly anisotropic directly transmitted radiation and first-order scattering in the source terms in (31) and (35) convey the memory of the laser-source's strong directionality. Otherwise ($E_d > 0$ and $E_c = 0$), that memory is immediately lost as soon as we enter the medium.

3.3 Boundary Conditions in Diffusion Theory

The reader has probably realized by now that in solar and lidar atmospheric RT problems, boundary layers are regions of vulnerability for diffusion theory as encapsulated in the assumption that (36) applies everywhere. Yet we need BCs for the coupled 1st-order PDEs we have now at hand. They must express in the "flux" language of diffusion theory, what radiation is entering the medium, or not.

We first turn to the diffusion theoretical expression in (36) for $G(ct, \boldsymbol{x}, \boldsymbol{\Omega})$ and compute hemispherical fluxes in both directions at both boundaries. We thus evaluate $F_z^{(\pm)}(ct, \boldsymbol{x})$ from (10), leading to:

$$F_z^{(\pm)}(ct, \vec{\rho}, 0) = J(ct, \vec{\rho}, 0)/4 \pm F_z(ct, \vec{\rho}, 0)/2, \tag{38}$$

$$F_z^{(\pm)}(ct, \vec{\rho}, H) = J(ct, \vec{\rho}, H)/4 \mp F_z(ct, \vec{\rho}, H)/2. \tag{39}$$

For the required BCs, we take $(+)$ at $z = 0$ and $(-)$ at $z = H$.

Following long-established tradition in the diffusion approximation to linear transport theory,[25] of which RT is just one example, we preemptively rewrite these boundary-crossing hemispherical fluxes as

$$F_z^{(\pm)}(ct, \vec{\rho}, 0) = [J(ct, \vec{\rho}, 0) \pm 3\chi F_z(ct, \vec{\rho}, 0)]/4, \tag{40}$$

$$F_z^{(\pm)}(ct, \vec{\rho}, H) = [J(ct, \vec{\rho}, H) \mp 3\chi F_z(ct, \vec{\rho}, H)]/4, \tag{41}$$

introducing χ as an $O(1)$ numerical factor that we can use to improve the diffusion model's accuracy w.r.t. to some benchmark result obtained from bone fide RT. Since the above BCs are statements about the incoming hemispherical fluxes $F_z^{(\pm)}$ there is indeed no compelling reason to impose Fick's law for $F_z = F_z^{(+)} - F_z^{(-)}$ at the boundary. If we did, we would find $\chi = 1/3$, which is too low.

Recalling that $F_z = -\partial_z J/3(\sigma_t + s)$ by Fick's law, it is clear why χ is called the "extrapolation scale" factor: it modulates the distance *outside* the medium at which J will take a BC-prescribed value using a linear approximation based on $(J, \partial_z J)$ at $z = 0$ or H. Based on (38)–(39), $\chi = 2/3$ is clearly a natural choice, and it is in fact required to conserve energy when $E_c > 0$ (and $E_d = 0$). However, other choices have been proposed and used when $E_d > 0$, such as $1/\sqrt{3} \approx 0.577$ and $0.7104\cdots$.

We now turn to the expressions for directional radiance in the RT BCs (8) and (9). Here, we find

$$F_z^{(+)}(ct, \vec{\rho}, 0) = E_d \delta(\vec{\rho}), \tag{42}$$

$$F_z^{(-)}(ct, \vec{\rho}, H) = \alpha F_z^{(+)}(ct, \vec{\rho}, 0). \tag{43}$$

Equating with appropriately signed flux in (40)–(41), we find:

$$J(ct, \vec{\rho}, 0) + 3\chi F_z(ct, \vec{\rho}, 0) = 4E_d \delta(\vec{\rho}), \tag{44}$$

$$(1 - \alpha) J(ct, \vec{\rho}, H) - 3\chi(1 + \alpha) F_z(ct, \vec{\rho}, H) = 0. \tag{45}$$

The above BCs at $z = 0, H$ carry over directly to the Laplace-transformed problem for $J(s, \vec{\rho}, z)$ and $F_z(s, \vec{\rho}, z)$.

3.4 Outgoing Boundary Fluxes from Diffusion Theory

In remote sensing, we are only interested in the outgoing boundary radiances, so here we are particularly in outgoing fluxes, $F_z^{(-)}(ct, \vec{\rho}, 0)$ for diffuse reflection and $F_z^{(+)}(ct, \vec{\rho}, H)$ for diffuse transmission (possibly including some direct as well if $E_d > 0$).

When sources are directional and internal ($E_\mathrm{c} = 1, E_\mathrm{d} = 0$) and the ground is black ($\alpha = 0$), we can define and evaluate

$$R(ct, \vec{\rho}) = F_z^{(-)}(ct, \vec{\rho}, 0)/E_\mathrm{c} = J(ct, \vec{\rho}, 0)/2E_\mathrm{c}, \tag{46}$$
$$T(ct, \vec{\rho}) = F_z^{(+)}(ct, \vec{\rho}, H)/E_\mathrm{c} = J(ct, \vec{\rho}, H)/2E_\mathrm{c}, \tag{47}$$

respectively, the normalized space-time reflection and transmission functions, where we combined the corresponding BC and hemispheric flux estimations. When sources are diffuse and confined to the boundary at $z = 0$ ($E_\mathrm{d} = 1, E_\mathrm{c} = 0$) and the ground is again black ($\alpha = 0$), we find

$$R(ct, \vec{\rho}) = F_z^{(-)}(ct, \vec{\rho}, 0)/E_\mathrm{d} = J(ct, \vec{\rho}, 0)/2E_\mathrm{d} - 1, \tag{48}$$

and the same expression for $T(ct, \vec{\rho})$ as in (47) but it now applies to total transmission. Although it will not amount to much in opaque diffusive media, this includes light coming directly from the diffuse source on the opposite side.

All of the above carries over immediately from functions of $(ct, \vec{\rho})$ to functions of $(s, \vec{\rho})$. We will revisit the case where $\alpha > 0$ using a different approach in §3.6.

3.5 Horizontally Fourier-Transformed Problem

Although we have carried so far the possibility of arbitrary horizontal variations with $\vec{\rho}$, lidar systems generally orient the transmitted beam vertically. So both types of source considered here are azimuthally symmetric, and so will be the Green functions they excite, i.e., they will depend only on $\rho = \|\vec{\rho}\|$. This rotational symmetry opens the possibility of a highly simplified problem after a horizontal Fourier transformation.

Consider the 2D horizontal Fourier transform of the already Laplace transformed $J(s, \vec{\rho}, z)$:

$$\tilde{J}(s, \vec{k}, z) = \iint_{-\infty}^{+\infty} J(s, \vec{\rho}, z) \exp\left(\mathrm{i}\vec{k} \cdot \vec{\rho}\right) \mathrm{d}\vec{\rho}. \tag{49}$$

We can write a similar expression for $\boldsymbol{F}(s, \vec{\rho}, z) = (\vec{F}_\mathrm{h}, F_z)^\mathrm{T}(s, \vec{\rho}, z)$. Recalling that Fourier transformation translates the gradient operator $\nabla = (\vec{\nabla}, \partial_z)^\mathrm{T}$ into $(\mathrm{i}\vec{k}, \mathrm{d}/\mathrm{d}z)^\mathrm{T}$, we Fourier transform the first-order coupled PDEs (31) and (35). After a little algebra, we are left with 2 coupled ODEs in z for $\{\tilde{J}, \tilde{F}_z\}$ instead of 4 coupled PDEs in $\boldsymbol{x}$ for $\{J, \boldsymbol{F}\}$:

$$\frac{\mathrm{d}\tilde{F}_z}{\mathrm{d}z} = -\left(\sigma_\mathrm{a} + s + k^2/3\sigma_\mathrm{t}\right) \tilde{J} + E_\mathrm{c}\sigma_\mathrm{s} \exp(-(\sigma + s)z), \tag{50}$$
$$\frac{\mathrm{d}\tilde{J}}{\mathrm{d}z} = -3\left(\sigma_\mathrm{t} + \zeta s\right) \tilde{F}_z + 3E_\mathrm{c}\sigma_\mathrm{s} g \exp(-(\sigma + s)z). \tag{51}$$

We can now view s and k^2 just as *parameters* in a 1D RT problem in z. Mathematically, this 1D RT problem is quite similar to the "delta-Eddington" version of the classic two-stream model used primarily in shortwave radiation budget estimation[26] in the special case of normally incident sunlight. Apart from the appearance of a total pulse energy E_c instead of the extra-atmospheric solar irradiance (often denoted by F_0), the problems are identical if we set $\zeta = 1$ and $k = 0$ (spatially-integrated observations only).

The BCs in (44)–(45) are straightforward to recast:

$$\tilde{J}(s, k^2, 0) + 3\chi\tilde{F}_z(s, k^2, 0) = 4E_\mathrm{d}, \tag{52}$$
$$(1 - \alpha)\tilde{J}(s, k^2, H) - 3\chi(1 + \alpha)\tilde{F}_z(s, k^2, H) = 0. \tag{53}$$

The simple expressions in §3.4 for R and T in $(ct, \vec{\rho})$-space carry over immediately to $(s, \vec{k})$ space, recalling that they are already customized for the case of black ($\alpha = 0$) surfaces.

An immediate advantage of having the 2D Fourier transform of steady-state ($s = 0$) outgoing boundary fluxes, $\tilde{F}(\vec{k})$ with $F = R, T$ is the capability of computing the non-vanishing (even-ordered) statistical moments of $\vec{\rho}$, the random horizontal transport distance upon escape away from the z-axis, which is aligned with the incoming laser beam. (By azimuthal symmetry, we know that odd-ordered moments, including the mean $\langle\vec{\rho}\rangle_F$, vanish identically.) Specifically, going back to (49), we can show that the variance

$$\langle\rho^2\rangle_F = \iint_{-\infty}^{+\infty} \vec{\rho}^2 F(0,\vec{\rho})\mathrm{d}\vec{\rho} \Big/ \iint_{-\infty}^{+\infty} F(0,\vec{\rho})\mathrm{d}\vec{\rho}, \tag{54}$$

for $F = R, T$, which can be evaluated from

$$\langle\vec{\rho}^2\rangle_F = \frac{-1}{\tilde{F}(0,\vec{0})}\vec{\nabla}^2\tilde{F}(0,\vec{k})\Big|_{\vec{k}=\vec{0}} = \frac{-2}{\tilde{F}(0,0)}\left(\frac{\mathrm{d}}{\mathrm{d}(k^2)}\right)\tilde{F}(0,k^2)\Big|_{k^2=0}. \tag{55}$$

In analogy with the similar process used in the time-domain in §2.4, we can identify

$$\left\langle \exp\left(\mathrm{i}\vec{k}\cdot\vec{\rho}\right)\right\rangle_F = \frac{\tilde{F}(0,k^2)}{\tilde{F}(0,0)} \tag{56}$$

as the Fourier-characteristic (or "moment-generating") function for $\vec{\rho}$, the random horizontal transport distance at escape.

As for the previously introduced Laplace-only transforms, we will drop in the remainder of the report the "tilde" notation for Fourier-Laplace transformed quantities. The distinction will be obvious by the context and/or the stated arguments.

3.6 Probabilistic Interpretations & Multiple Surface Reflections

In the 2+1D physical space spanned by $(ct, \vec{\rho})$, ct is the random pathlength upon escape that describes the stretching of the incoming laser pulse by multiple scattering and $\vec{\rho}$ the random horizontal transport distance upon escape away from the incoming laser beam. Consequently, $F(ct, \vec{\rho})$ with $F = R, T$ is a joint form of the "impulse response function" (IRF) of the medium to a delta-in-time source at a boundary (usually presumed spatially uniform), and its "point spread function" (PSF), defined as the response of the medium to a delta-in-space source at a boundary (usually presumed steady in time). That makes $F(s, \vec{k})$ with $F = R, T$ a joint Laplace frequency response function (LRF) and modulation transfer function (MTF) for the medium of interest.

Focusing on overall reflection, how does the presence of a reflecting surface affect these random variables? The light can bounce (partially, when $\alpha < 1$) off the ground any number of times: 0,1,2,3,$\cdots$. Each time it does, it is as if, after a certain amount of scattering, a secondary source appears at the ground at some random value of $(ct, \vec{\rho})$ and the transport process through multiple scattering starts again, but from an *isotropic* source on hte opposite side of the medium. The random outcome in $(ct, \vec{\rho})$ at $z = 0$ after one surface reflection is the sum of two random variables for transmission, first for a collimated source, then for a diffuse source, modulated by the probability of ground reflection ($0 < \alpha \leq 1$). But the medium can itself reflect the bounced (isotropic) light back to the surface for another reflection, thus adding more random space-time variables, and so on.

Formally, this can be written as an infinite sequence of space-time convolutions. Specifically, for the overall reflection back to the region where the laser light comes from, we have:

$$\begin{aligned} R &= R_\mathrm{c} + T_\mathrm{c} * \left(\alpha T_\mathrm{d} + \alpha^2 R_\mathrm{d} * T_\mathrm{d} + \alpha^3 R_\mathrm{d} * R_\mathrm{d} * T_\mathrm{d} + \cdots\right) \\ &= R_\mathrm{c} + T_\mathrm{c}\alpha(1 - \alpha R_\mathrm{d})^{-1} T_\mathrm{d}, \end{aligned} \tag{57}$$

where $F_{\mathrm{c,d}}$ ($F = R, T$) are the space-time responses respectively for collimated and diffuse boundary sources, and all the products of functions of $(ct, \vec{\rho})$ are in fact convolution products, denoted here by $*$ (only in the first line).

Fortunately, there are Fourier- and Laplace theorems stating that the characteristic function of a sum of random variable is the (standard) product of the characteristic functions of all the random variables. Moreover, this generalizes to higher dimensions, and even to heterogeneous spaces such as $\mathbb{R}^+ \otimes \mathbb{R}^2$ spanned by $(ct, \vec{\rho})^{\mathrm{T}}$.

Consequently, the second line in (57) can be used as is for the Fourier-Laplace transformed multi-variate response functions. Moreover, this only calls for the "black surface" quantities estimated in §3.4 (after Fourier–Laplace transformation). This solves the most general problem we have in mind for the present investigation on new lidar equations for multiple scattering in opaque natural media. We now examine a few applications.

4. NEW LIDAR EQUATIONS AT WORK IN OPAQUE NATURAL MEDIA

4.1 "Crude" Versus "Refined" Diffusion Theories

The analytical solutions of diffusion models have always been and will continue to be evaluated against numerical solutions of the full time-dependent 1D RTE using, until further notice, Monte Carlo techniques. However, among diffusion models there are several levels of anticipated accuracy with respect to the full RTE solutions. The telegrapher's equation ($\zeta = 1$) is better than the classic diffusion equation ($\zeta = 0$). It is better to use $E_{\mathrm{c}} = 1$ and $E_{\mathrm{d}} = 0$ (collimated internal sources) than $E_{\mathrm{d}} = 1$ and $E_{\mathrm{c}} = 0$ (isotropic boundary sources).

There is an easy way to improve some of the better diffusion models using collimated internal sources, namely, by invoking the δ-Eddington scaling.[27] This starts with the remark that one can take a fraction $f \in (0, 1)$ of the phase function in (37) and put it into a Dirac δ at $\theta_{\mathrm{s}} = 0$, thus effectively replacing forward scattering by no scattering. Holding the overall g constant, the renormalized phase function has a lesser asymmetry factor

$$g' = \frac{g - f}{1 - f}. \tag{58}$$

Accordingly, extinction is replaced by

$$\sigma' = (1 - f\varpi_0)\sigma, \tag{59}$$

and SSA by

$$\varpi_0' = \frac{1 - f}{1 - f\varpi_0}\,\varpi_0. \tag{60}$$

A popular choice for f is g^2, which reduces $g' = g/(1 + g)$ to the interval $(0, 1/2)$, based on energy budget considerations. With that rational choice, we also find that

$$\sigma_{\mathrm{a}}' = \sigma_{\mathrm{a}}, \tag{61}$$

$$\sigma_{\mathrm{t}}' = \sigma_{\mathrm{t}}. \tag{62}$$

These properities are thus invariant under δ-Eddington scaling. It immediately follows that the ($s = k^2 = 0$) albedo for diffuse boundary source diffusion models, with $E_{\mathrm{c}} = 0$ and $E_{\mathrm{d}} > 0$, is not affected since it is a function only of σ_{a} and σ_{t}. But models with distributed internal anisotropic sources ($E_{\mathrm{c}} = 0$ and $E_{\mathrm{d}} > 0$) should see some improvement since $g' < g$. The multiple scattering diffusion model per se is now tasked with a more isotropic scattering and a more isotropic source.

There are also potentially worse models than used here so far, although to what extent has yet to be assessed. An example is to use instead of the exact diffusion BCs in (44)–(45) "extended" ones for the 2nd-order ODE that results from the elimination of F_z between (50) and (51) for classic ($\zeta = 0$) diffusion theory. Specifically, we obtain a Helmoltz or (screened) Poisson-type equation,

$$\left[\frac{\mathrm{d}^2}{\mathrm{d}z^2} + 3\sigma_{\mathrm{t}}\left(\sigma_{\mathrm{a}} + s + k^2/3\sigma_{\mathrm{t}}\right)\right] J = \left\{ \begin{array}{l} 0 \\ E_{\mathrm{d}} \exp(-s/\sigma_{\mathrm{t}})\delta(z - 1/\sigma_{\mathrm{t}}) \end{array} \right. , \tag{63}$$

for which we use the Dirichlet (rather than exact Robin or "mixed") BCs:

$$J(-\chi/\sigma_{\mathrm{t}}) = \left\{ \begin{array}{l} 4E_{\mathrm{d}} \\ 0 \end{array} \right. , \tag{64}$$

$$J(H + \chi/\sigma_{\mathrm{t}}) = 0, \tag{65}$$

where $\chi\ell_t = \chi/\sigma_t$ is the extrapolation length. We have here two variants. The upper expressions on the right-hand sides of (63) and (64) mimic the isotropic boundary source model ($E_c = 0$ in previous versions). The lower expressions mimic the idea of internal source ($E_c > 0$ in previous versions). However, rather than an anisotropic source distributed along the z-axis, as in (50)–(51), one can reduce it to an isotropic source at one transport MFP ($\ell_t = 1/\sigma_t$) into the medium. Going back to Fig. 1, we now note that the black symbol is placed at exactly one transport MFP (0.22 km) into the cloud. It seems to be a good position for an isotropic source to create roughly the same far-field radiance pattern.

A demonstrated[28] advantage of these approximate diffusion models in (63)–(65) is that the resulting closed-form solutions are invertible Laplace- and Fourier transforms in the form of infinite series, one appropriate for early times and short off-axis distances, and another far more interesting one for the opposite asymptotic limit.

Now, in the following, we seek only the basic information content of a given multiple scattering lidar observation based on the new equations. In our experience, even the most basic diffusion model delivers the right qualitative answer. We will therefore proceed with any convenient model. Table 2 shows the options used in the following case studies.

Table 2. Features of the diffusion models used in the cases studies. In the bathymetry study, the only one with a partially reflecting surface (cf. Table 1), requires responses for both collimated and diffuse illuminations, as evidences in (57). (So $E_d = 1$ here is not used as an approximation.)

Parameter:	ζ	E_c	E_d	Extended BCs	δ-Eddington
Stratiform clouds	0	0	1	no	no
Absorbing aerosol plumes	1	0	1	no	no
Dirty snow	0	0	1	no	no
Bathymetry & turbidity	0	1	(1)	no	yes

4.2 Stratiform Clouds

Although multiple scattering lidar has not been adopted as an operational approach in cloud remote sensing, these natural media have been the subject of conclusive pilot studies using the new technology. These studies demonstrated that stratiform clouds—extensive unbroken layers that approximate the assumed plane-parallel slab geometry—can be remotely probed with multiple scattering lidar. In §2.2, we mentioned three case studies: ground-based WAIL, airborne THOR, and space-based LITE.

The first two came to fruition at a successful joint field campaign conducted in March 2004 at the DOE's Atmospheric Radiation Measurements (ARM) facility in Norman, Oklahoma.[10,11] WAIL data was used to derive the pair $\{H, \tau\}$ for two collections with the prototype system built at Los Alamos National Laboratory (LANL). The cloud property retrieval used a parametric diffusion-based forward model predicated on (63)–(65) followed by inverse Fourier–Laplace transforms. The WAIL data was indeed limited to Green function observations that were highly truncated spatially due to a combination of insufficient FOV (even at 54°) and low cloud base (at ≈0.5 km), thus precluding methods based on empirical estimates of the statistical moments in (18) and (54). That same night in March 2002, THOR operated nominally at 8–9 km above data top. Its data was used to derive many values of H for the same cloud deck using a neural network to infer cloud properties from a large number of Monte Carlo simulations. THOR data collected during that 2004 deployment was recently revisited with a promising new forward model akin to diffusion[29] and a variational data analysis methodology inspired by data assimilation.[30] The cloud properties delivered by both WAIL and THOR compared well with those measure directly by ARM instruments or, in the case of THOR, objectively extended from these to the whole region where the overflight was performed using the meteorological situation.

Interestingly, LITE preceded THOR and WAIL by almost 8 years. It was a historically important and deliberate demonstration of lidar technology in space that has since be followed by the ICESat[31] and CALIPSO[32]

missions, with more to come. However, as a test of multiple scattering lidar in clouds, LITE was largely inadvertent: instrument parameters, essentially unchanged from a large upward-looking system targeting aerosols, were just right for looking down at clouds.[33]

One more active optical instrument development project with a closely related signal physics was not mentioned in §2.2 because it is not a remote sensing technique per se: in situ cloud lidar.[34,35] In this alternative airborne method a pulse laser is fired horizontally out of a window of a LearJet (instrumented for probing cloud particles directly from inside the cloud) and highly scattered laser light is gather by relatively wide FOV non-imaging sensors looking up and down from the tip of the wing on the opposite side of the aircraft. The data analysis also used numerical Monte Carlo results (for stochastic cloud models with 3D spatial variability) that were inverse-mapped to cloud properties (plus aircraft location between boundaries) using a neural network. The airborne technology demonstration was highly successful and the inversion technique was validated against other cloud probes on a mountain-top facility.

Before moving on to our physics-based information content analysis of multiple scattering lidar using diffusion-theoretical methods for clouds and beyond, we must draw the readers attention to the fact that all of the above cloud observations were performed at night, and this was key to their success. Daytime observations of the relatively weak multiply scattered laser light at significant distances from the beam will be a challenge that can only be addressed by using rather sophisticated filtering methods to reject the solar background. A preliminary lab study is described by Love et al.[22]

To kick off the theoretical assessment of the data worth mining in multiple scattering lidar systems adapted for a number of opaque natural optical media listed in Table 1, we start with clouds even if the proof-of-concept is in for the hardware as well as for data analysis methods.

Going back to the first dedicated paper on multiple scattering cloud lidar by Davis et al.,[36] the simplest kind of diffusion model was used and the instrument was assumed "perfect" in the sense that its data is good enough to estimate $\langle (ct)^q \rangle$ in (18)) for $q = 1$ and 2, $\langle \rho^2 \rangle$ in (54), and possibly also the spatial and temporal integral of the Green function, a.k.a., cloud albedo

$$R = \frac{1}{E_{\mathrm{c/d}}} \int_0^\infty \iint_{-\infty}^{+\infty} G(ct, \vec{\rho}) \mathrm{d}ct \mathrm{d}\vec{\rho} = \tilde{R}(s, k^2)\Big|_{s,k=0}, \tag{66}$$

which would call for absolute radiometric calibration. The statistical moments of the Green function, being ratios of integrals are not dependent on radiometric calibration, i.e., do not care about the value of $E_{\mathrm{c/d}}$. As long as responses are linear in radiometry and uniform in space and time, we can estimate the moments accurately. We revert to these simple premises for the reminder of the paper on the basis that, so far, they correctly predicted what can be done with a real multiple scattering lidar system. At any rate, they are good enough to evaluate the need for deeper investigation.

We therefore solve the simple ODE problem in (50)–(53) with:

- $\sigma_{\mathrm{a}} = 0$, expressing that there is no absorption by water droplets or crystals (say, by choosing to use a green laser source);
- $\zeta = 0$ (no need for the telegrapher's equation);
- $E_{\mathrm{d}} = 1$, diffuse boundary sources suffice (hence $E_{\mathrm{c}} = 0$); and
- $\alpha = 0$, black surface (approximating water).

This gives us the pair of functions $\{J(z), F_z(z)\}$, from which we only need to compute the Fourier-Laplace transform of the reflected flux (48), namely,

$$R(s, k^2) = \frac{J(s, k^2)}{2} - 1 = \frac{[1 - (k^2/\sigma_{\mathrm{t}} + 3s)]\chi^2}{[1 + (k^2/\sigma_{\mathrm{t}} + 3s)]\chi^2 + 2\sqrt{k^2/\sigma_{\mathrm{t}} + 3s}\chi \coth(H\sigma_{\mathrm{t}}\sqrt{k^2/\sigma_{\mathrm{t}} + 3s})}. \tag{67}$$

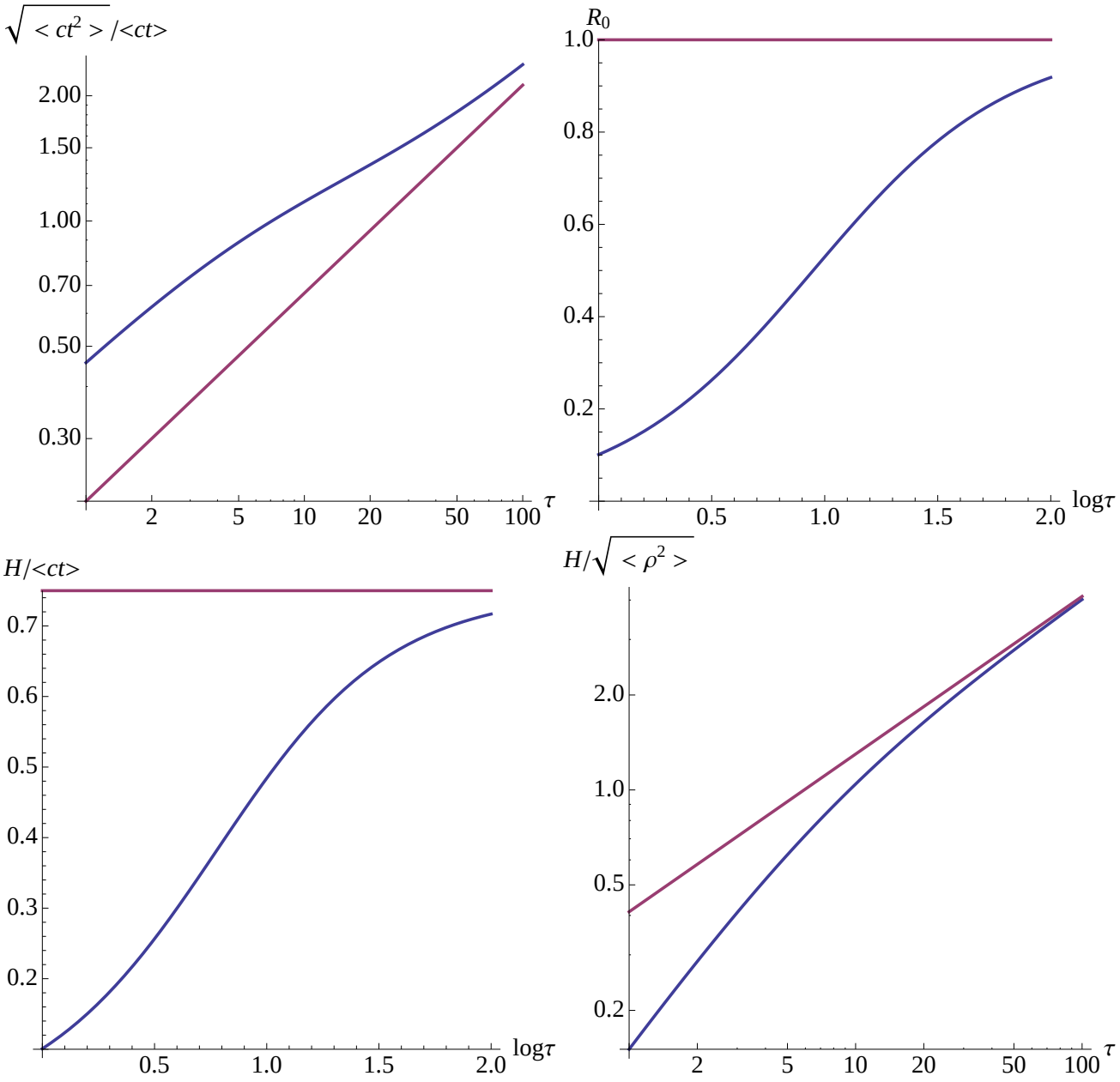

Figure 2. Utilization of three moments from a cloud's Green function in space and/or in time, along with its albedo R_0, to infer the two basic cloud properties $\{H, \tau\}$. See discussion of several possible approaches in main text.

The change of variables to the more common parameterization of cloud optical properties is straightforward: $\sigma_t = (1-g)\sigma$ (where $g \approx 0.85$ for liquid water clouds), where $\sigma = \tau/H$.

From there, we get the cloud albedo

$$R_0 = R(0,0) = \frac{(1-g)\tau}{2\chi + (1-g)\tau}, \tag{68}$$

a classic result from two-stream theory.[37] By estimating derivatives of (67) at $s, k^2 = 0$, we obtain the Green function moments of interest:

$$\langle ct \rangle = 2\chi H \times (1 + C_1[(1-g)\tau/2\chi]), \tag{69}$$

$$\langle (ct)^2 \rangle = \frac{4}{5}\chi H^2 (1-g)\tau \times (1 + C_2[(1-g)\tau/2\chi]), \tag{70}$$

$$\langle \rho^2 \rangle = \frac{4}{3}\frac{\chi H^2}{(1-g)\tau} \times (1 + C_1[(1-g)\tau/2\chi]), \tag{71}$$

where we have highlighted the asymptotic scaling with the key cloud properties $\{H, (1-g)\tau\}$; pre-asymptotic corrections are

$$C_1(X) = \frac{3+2X}{4X(1+X)}, \tag{72}$$

$$C_2(X) = \frac{45 + 2X(75 + 82x + 32X^2)}{16X^2(1+X)^2}, \tag{73}$$

which both vanish as $1/X$ when $X \to \infty$. We note that they are identical for $\langle ct \rangle$ and $\langle \rho^2 \rangle$, which follows from the equivalent roles in (67) of s and $k^2/3\sigma_t$. In fact, this similarity relation can be used to translate the leading terms for $\langle ct \rangle$ into those for $\langle \rho^2 \rangle$ using $\sigma_t = (1-g)\tau/H$.

We consider the left-hand sides of (69)–(71) to be the multiple scattering lidar observables that do not require calibrated radiometry. Any pair of these expressions for moments can be used to solve for $\{H, \tau\}$, knowing that $g \approx 0.85$. We note here—and this remains true for the remainder of the paper—that since we are using only "marginal" moments (i.e., observations) either of pathlength or of horizontal transport distance, the sensors we need in practice can be quite simple. They consist only of:

- a standard lidar receiver for measuring returned pulses, but fed with a fore-optics with a wide-enough FOV for estimating $\langle (ct)^q \rangle$ $(q = 1, 2)$, and
- a flat-fielded digital camera, also with a sufficiently wide FOV for estimating $\langle \rho^2 \rangle$.

If that never-easy radiometric calibration is available, it is probably by using a collocated passive sensor for diffusely reflected solar radiation. In that case, we can also use R_0 in (68) or, if it is a ground-based station, we can equally well use the cloud's transmittance $T_0 = 1 - R_0 = 1/(1 + (1-g)\tau/2\chi)$. But it is interesting to note that scaled cloud optical depth $(1-g)\tau$ can be obtained from non-calibrated data used to form the above moments or, better still, moment ratios that do not even involve H.

All four cloud responses in (68)–(71) have been used to produce the four panels in Fig. 2 where we have set $g = 0.85$ and $\chi = 2/3$. On the top row, we show two non-dimensional monotonic functions of τ; either one can be used to obtain that non-dimensional cloud property. However, on the right, we find $R_0(\tau)$, which calls for a well calibrated radiometer. On the bottom row, we find non-dimensional ratios $H/\langle ct \rangle$, and $H/\sqrt{\langle \rho^2 \rangle}$; one or the other can be used to derive H knowing respectively the mean pathlength or the RMS horizontal displacement. Their asymptotic trends in τ are indicated throughout.

The two observations used on the left of Fig. 2 suffice to infer $\{H, \tau\}$, and they use only a standard lidar detector with adapted fore-optics, without a need for calibration. The same is true of the two observations used on the right, but the one for R_0 (top panel) calls for absolute radiometric calibration. In compensation for that complication, the instrument used to obtain $\langle \rho^2 \rangle$ can be as simple as a digital camera since there is no need for resolving the time-dependence: one only needs to image the spatial Green function.

4.3 Extended Aerosol Plumes

Here we simply ask if we can extend the simple study of cloud property feasibility to the case of dense plumes of absorbing aerosol such as

- dust, lofted and transported away from source regions;
- volcanic ash;
- smoke, from wild fires and biomass burning.

This capability would be of considerable interest to applied scientists focussing on the climate impacts of aerosols, air quality monitoring and forecasting, and aviation safety.

In terms of remote sensing and the forward radiative transfer modeling, we simply want to add the SSA ϖ_0 to the two cloud unknowns $\{\tau, H\}$. To explore this possibility, again adopt a simple diffusion model in (50)–(53) with $E_{\rm d} = 1$ (hence $E_{\rm c} = 0$), $\zeta = 1$ (telegrapher's problem), $\alpha = 0$, and now allow for $\sigma_{\rm a} > 0$. However, it is intuitively clear that diffusion theory, which thrives on scattering, cannot account accurately for strong absorption. SSA values less than 0.9 would be risky. Yet absorbing aerosols can have lower values of ϖ_0. However, we recall once more that we are not trying here to build a quantitatively accurate model, say, to analyse real data. Rather, we wich to draw qualitative conclusions about information content of some given multiple scattering lidar observations.

The outcome of the computation for $R(s, k^2)$, also a function of the parameter set $(H, \sigma_{\rm t}, \sigma_{\rm a}, \chi)$, is as in (67) but more complex. The subsequent change of variables also needs to be modified: $\sigma_{\rm a} = (1-\varpi_0)\sigma$, $\sigma_{\rm t} = (1-\varpi_0 g)\sigma$ (where g is smaller for aerosols than for liquid water clouds), and $\sigma = \tau/H$. We again take $\chi = 2/3$ and set $g = 0.75$, a typical value for fine-mode aerosols.

Under these assumptions, Fig. 3 shows the same four basic responses used in Fig. 2, but this time as a function of $\log\tau$ and ϖ_0. We let, with some trepidation, the latter SSA parameter vary from unity down to 0.7, which at least begins to capture the absorbing aerosol SSA values found in nature. Although we are still very interested in the plumes geometrical (H) and optical (τ) thicknesses, SSA is the highest value target because it is very informative about the particulate's chemistry and history. Not to mention the fact that SSA controls the poorly-understood "semi-direct" effect of aerosols on the climate system, by which they heat the atmosphere and potentially change its thermal structure enough to inhibit cloud formation.

The best way to read Fig. 3, which displays the four functions of $(\varpi_0, \log\tau)$, is to inspect the isolines of non-dimensional moment ratios (top row) and, if necessary, albedo (lower right), two-by-two. We seek regions where the families of isolines intersect each other at the largest possible angle. That way, we can pinpoint $(\varpi_0, \log\tau)$ with two judicious observations. Then the fourth function, in this case, again $H/\langle ct\rangle$, can be used to translate the observed $\langle ct\rangle$ into an estimate for H.

The only region of $(\varpi_0, \log\tau)$-space with some degree of iso-line orthogonality in the top row is at low τ ($\lesssim$3) and low ϖ_0 ($\lesssim$0.9). This is not where diffusion works the best and in fact, the standard 1D RT models used in operational aerosol retrievals still work relatively well, which does not mean it is easy to tease out the absorption (hence SSA) from the scattering. There is hope that polarization will help that cause.[38,39]

The good news is that multiple scattering moment ratios in the top row of Fig. 3 are sensitive to SSA (and only SSA) in the optically thick regime where the operational aerosol algorithms invariably fail. Therefore, although this is also the case for the existing sensors measuring R, it can be done with a multiple scattering lidar system without the need for radiometric calibration. Specifically, in the limit $\tau \to \infty$, we can use the $g = 0.75$ results in Fig. 5 below (computed however using $\zeta = 0$) for getting ϖ_0 from $\sqrt{\langle (ct)^2\rangle}/\langle ct\rangle$. Alternatively, we can use

$$\begin{aligned}\lim_{\tau\to\infty} \frac{\langle \rho^2\rangle}{\langle ct\rangle^2}(\varpi_0, g, \tau) &= \frac{2\sqrt{(1-\varpi_0)(1-\varpi_0 g)}\,\big(3(1-\varpi_0)\chi^2 - (1-\varpi_0 g)\big)}{27(1-g)^2\varpi_0^2\chi} \\ &\times \left(\frac{\sqrt{3}g\varpi_0 - 6\chi\sqrt{(1-\varpi_0)(1-\varpi_0 g)} - \sqrt{3}\,\big(1+3(1-\varpi_0)\chi^2\big)}{(1-\varpi_0 g) + 2\sqrt{3}\chi\sqrt{(1-\varpi_0)(1-\varpi_0 g)} + 3(1-\varpi_0)\chi^2}\right)^3, \end{aligned} \tag{74}$$

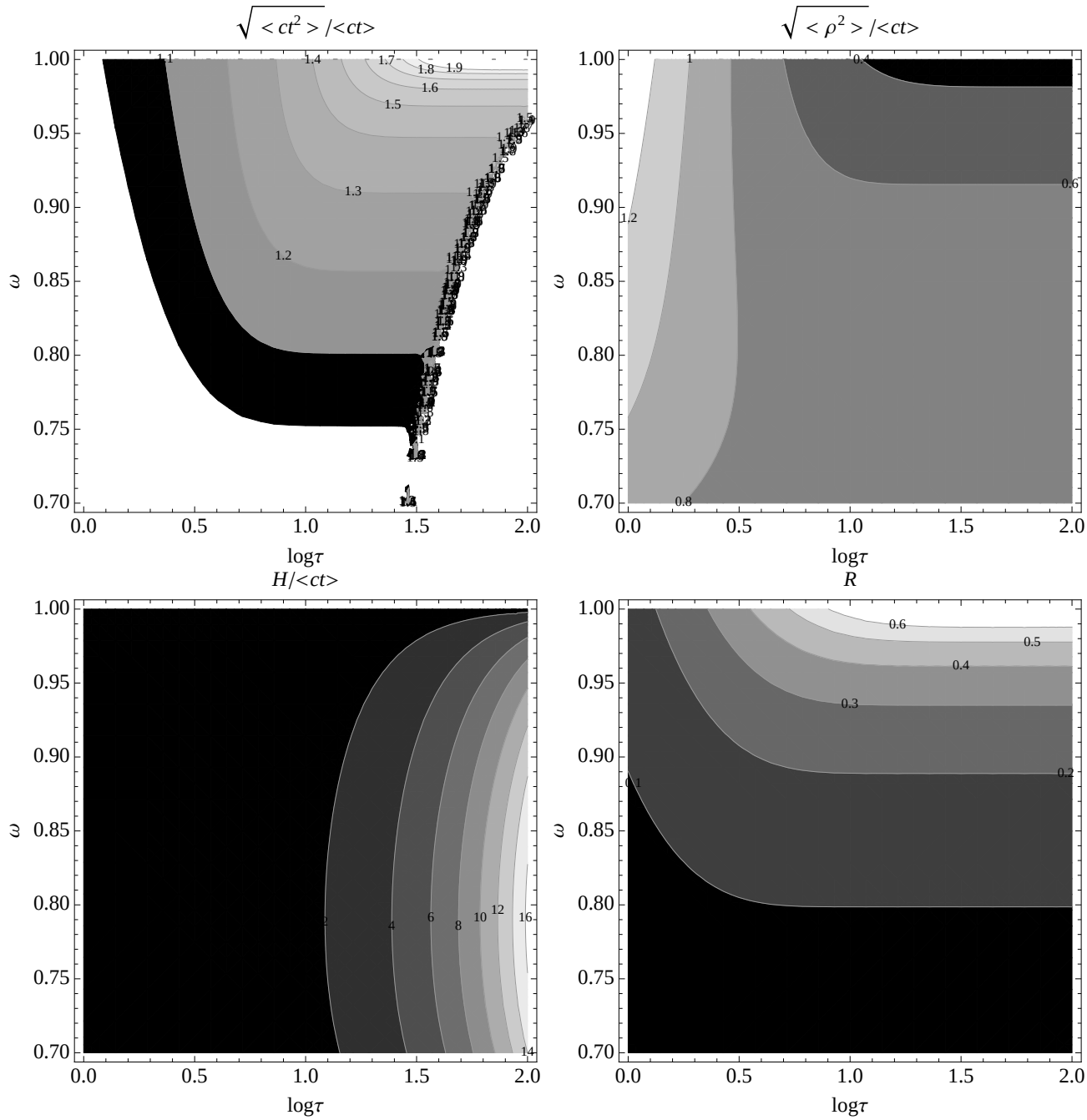

Figure 3. Utilization of three moments from an aerosol plume's Green function in space and/or in time, plus its albedo R, to infer the three basic aerosol plume properties $\{H, \tau, \varpi_0\}$. In the upper-left panel, we notice the high-τ/low-ϖ_0 region where there was a singularity for $\langle (ct)^2 \rangle / \langle ct \rangle^2$. Also, we only plot the region where Schwartz's inequality, $\langle (ct)^2 \rangle \geq \langle ct \rangle^2$, is verified by the predictions of this simple 3+1D RT model. See further discussion in main text.

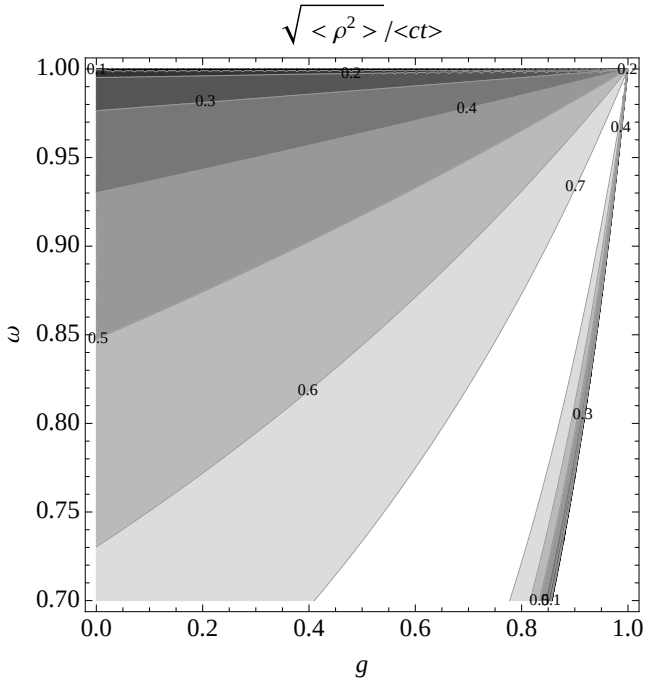

Figure 4. Asymptotic ($\tau \to \infty$) limit for $\langle \rho^2 \rangle^{1/2} / \langle ct \rangle$ from (74). For most, but not all, values of g, this function of ϖ_0 (denoted ω) is monotonic and can thus be used to estimate SSA from non-calibrated multiple scattering lidar data. See further discussion in main text.

which is plotted in Fig. 4, to solve (numerically) for ϖ_0, given g and χ. That done, the lower left-hand panel in Fig. 3 and the observed $\langle ct \rangle$ (or $\sqrt{\langle \rho^2 \rangle}$) gives us a one-to-one nonlinear connection between τ and H.

In conclusion, it seems that it will be difficult to jointly retrieve the trio of absorbing aerosol plume parameters $\{\varpi_0, \tau, H\}$ from a multiple scattering lidar system since absorption dominates the signals. That said, one should be able to estimate ϖ_0 approximately, and without relying on radiometric calibration. From there, one can determine a nonlinear relation between H and τ.

4.4 Snow and Sea Ice

For a detailed feasibility study on probing snow and sea ice with multiple scattering lidar, with an airborne system in mind, we refer the interested reader to the paper by Várnai and Cahalan.[40] Their investigation is based on numerical Monte Carlo solutions of the forward Green function problem, including a realistic (e.g., noisy) instrument model. In the absence of absorption, this problem is not fundamentally different from the cloud problem. Therefore, unsurprisingly, the authors find that H, and we suspect possibly also τ, can be inferred using a THOR-like system. These authors followed up on their numerical investigation with some simple experiments.[41]

Várnai and Cahalan bring up the issue of absorption by aerosol particles trapped in the snow, which we address here head-on using another diffusion model. We approximate the dirty snow layer with a semi-infinite scattering medium that also has some absorption. Specifically, we solve

$$\mathrm{d}F_z/\mathrm{d}z = -\left(\sigma_\mathrm{a} + s + k^2/3\sigma_\mathrm{t}\right) J, \tag{75}$$

$$\mathrm{d}J/\mathrm{d}z = -3\sigma_\mathrm{t} F_z, \tag{76}$$

for $\{J, F_z\}(z)$, as we did for clouds, but with BCs $J(0) + 2\chi F_z(0) = 4$ and now $\{J, F_z\}(z) \to 0$ as $z \to \infty$. The outcome is

$$R(s, k^2) = \frac{J(s, k^2)}{2} - 1 = \frac{\sigma_\mathrm{t} - \chi\sqrt{k^2 + 3(s + \sigma_\mathrm{a})\sigma_\mathrm{t}}}{\sigma_\mathrm{t} + \chi\sqrt{k^2 + 3(s + \sigma_\mathrm{a})\sigma_\mathrm{t}}}, \tag{77}$$

which we follow by the usual change of variables: $\sigma_a = (1 - \varpi_0)\sigma$ and $\sigma_t = (1 - \varpi_0 g)\sigma$.

Figure 5 shows three multiple scattering lidar responses, plus overall albedo, derived from (77) as functions of ϖ_0 and g. All panels here, as well as Fig. 4, show a strong sensitivity to ϖ_0 as it approaches unity, and this is made clear in (74) with the prominent $\sqrt{1 - \varpi_0}$ factor. On the left, we have the time-dependent responses, and on the right their steady-state counterparts. Knowing one moment along with the pair $\{\varpi_0, g\}$, one can use the appropriate bottom plot to obtain the extinction σ. However, the iso-lines in the two panels in the top row have very similar patterns, which means that we'll need to make an assumption about g in order to get ϖ_0, the high-value remote sensing target. Fortunately, there is robust knowledge of the scattering properties of snow particles.[42]

4.5 Bathymetry in Highly Turbid Shallow Waters

Lidar is increasingly used to generate 3D maps of terrain, as well as built environments.[43] All that is needed is to know precisely the position of the pulsed laser source and the direction it is pointing at, and detect the strong return from the ground or building. Ranging does the rest. Above-ground vegetation gives detectable returns but these false alarms for terrain detection are easily filtered in the time domain:[44] we are interested only in the last return, even if it is weakened. The same technology can be used to map the terrain underwater (laser bathymetry), correcting for refraction at the air-water interface.[45]

However, all of this assumes there is a detectable return coming *directly* from the target, be it the ground, a building, or the sea floor. But coastal or river waters are often highly turbid, heavily laden with suspended particulate matter known as "hydrosols," as well as aquatic plants. We view this "cloudiness" of the water as a candidate for deep penetration with multiple scattering lidar technology. Like aerosols, the hydrosols can be absorbing but, unlike any of the prior applications, there is a necessarily a partially reflective surface underlaying the medium.

We can use the same methodology as in the previous case studies to see if multiple scattering lidar can be of help. We have set the problem up using the summed expansion in multiple surface reflections in (57) when surface albedo $\alpha > 0$. Therefore, we need to compute both reflection and transmission functions dependent on (s, k^2), apart from parameters that define the medium. We need to do this, one at a time, for both collimated ($E_c = 1$) and diffuse ($E_d = 1$) sources. In the former case, we have activated δ-Eddington rescaling of g and tau. Hydrosol phase functions are highly forward-peaked, with $g = 0.96$ being a typical value, which leads to $g' \approx 0.49$ in (58) with $f = g^2$, very near the theoretical limit of 1/2.

Even assuming, for simplicity, that the hydrosols are non-absorbing ($\sigma_a = 0$), the resulting expressions are increasingly complex as we go from albedo to mean path and RMS horizontal transport to higher-order moments. But modern computer-assisted symbolic math applications can handle them. Apart from the sea floor's albedo α, the remote sensing unknowns are τ, the optical depth of the water and, most importantly, the water depth H.

Figure 6 shows the usual line-up of multiple scattering lidar responses, plus the albedo of the volume/surface system. With three unknowns, we will need all three moments to work properly for us. By that, we mean that the iso-lines of moment ratios (top row panels) need to have intersecting flows in interesting parts of the two-dimensional optical parameter space $\{\alpha, \tau\}$. This is indeed the case, at least in the intermediate τ region, especially for the higher α's. However, it is fair to say that both moment ratios in the top row are primarily functions of τ at the higher values of particular interest here. This is therefore a situation where radiometric calibration, hence access to R_0 would be very helpful to position the medium in $(\{\alpha, \tau\})$ space. The good news is that this could be done with a non-imaging wide-FOV system, using only the left-hand and lower-right panels. Only the new fore-optics need to be provided to implement the "multiple-scattering" channel.

In the upper left panel displaying $\sqrt{\langle (ct)^2 \rangle}/\langle ct \rangle$, we note that the diffusion model predicts numbers that are less than unity, thus violating Schwartz's inequality in probability theory, at optical depths below ≈10. This is a reminder that, unlike RT theory, diffusion theory is not sufficiently constrained to ensure either causality ($\sqrt{\langle \rho^2 \rangle}$ can exceed ct at early times) or positive definite solutions, i.e., the diffusion theoretical predictions for boundary-source/boundary-viewing Green functions are not necessarily valid PDFs for the probability of escape at $(ct, \vec{\rho})$. This is a shortfall for the model were it to be applied to real-world data analysis, but it does not

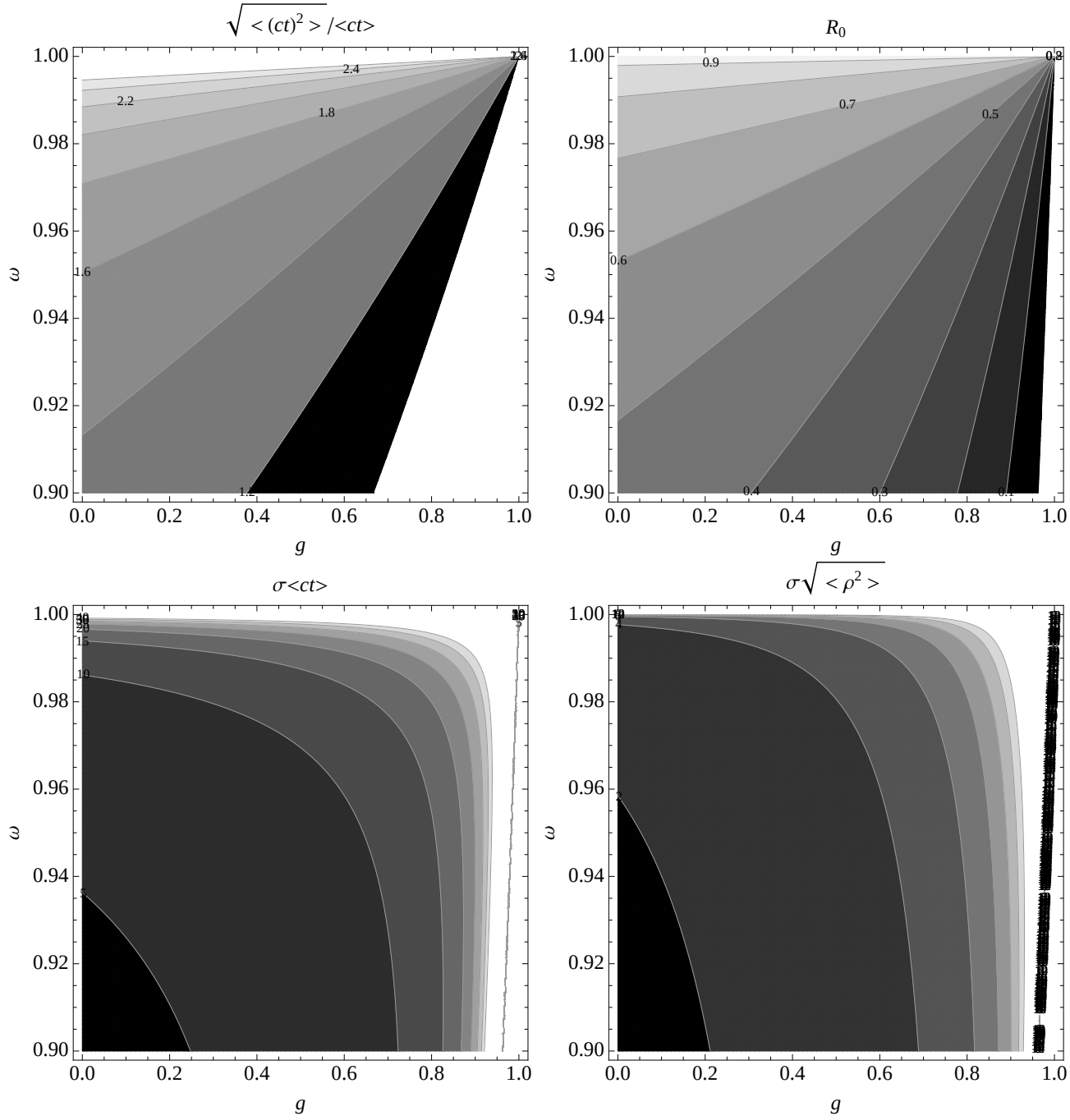

Figure 5. Utilization of three moments from the Green function in space and/or in time, plus albedo R_0, for a semi-infinite layer of dirty snow to infer the two basic properties $\{\varpi_0, g\}$ (with ω denoting ϖ_0). Another potentially useful moment ratio, $\sqrt{\langle (ct)^2 \rangle}/\langle ct \rangle$, computed (using $\zeta = 1$) for the semi-infinite scattering and absorbing medium is displayed in (74) and Fig. 4. More discussion in main text.

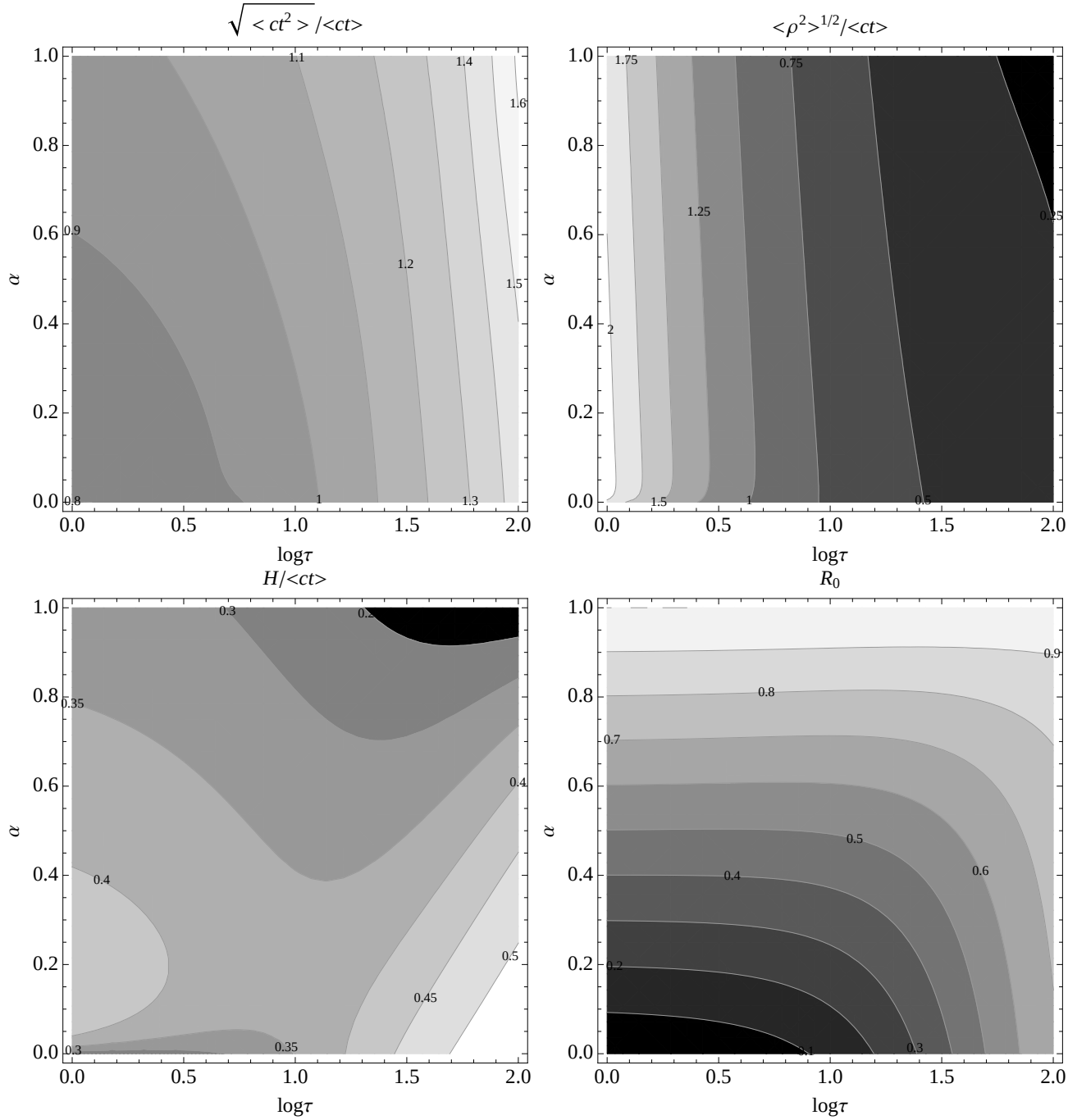

Figure 6. Utilization of three moments from the Green function in space and/or in time, in addition to albedo R_0, to infer three basic properties of an expanse of shallow but turbid coastal water, including its depth H and two optical properties τ and α. We assume, for simplicity, that $\varpi_0 = 1$ (no absorption by particulates in water) and that $g = 0.96$ (leading to a rescaled value of $g' = 0.49$). Actual computations use g' and $\tau' = (1 - g) \times \tau$ from the horizontal axis. See main text for further discussion.

invalidate the general parametric trends it predicts nor the exploitation we make of them here, namely, to extract the general information content of multiple scattering lidar signals.

At any rate, knowing where we are in (α, τ) space enables us to use the lower left panel to convert $\langle ct \rangle$ into an estimate of water depth H.

5. SUMMARY & OUTLOOK

In summary, I have laid down the physical foundations for building predictive forward models for multiple scattering lidar systems. First, I brought radiative transfer theory to bear. In a nutshell, multiple scattering lidars are designed to observe those space-time Green functions of the probed optical medium that are visible from the illuminated boundary. Then I used the asymptotic approximation for optically thick media, namely, radiative diffusion theory. Several further or lesser approximations are also introduced. The diffusion modeling framework is used here to predict in closed-form the dependence of spatial and temporal moments of the Green function on the parameters of the medium. In turn, these analytical expressions were use to determine the information content of the multiple scattering data, at least from ideal instruments. Several specific applications were revisited or explored here for the first time.

Specifically, we looked back at multiple scattering lidar accomplishments as emerging cloud remote sensing tools, explaining post-facto why the actual (less-than-ideal) instruments produced data from which cloud thickness and optical depth were inferred. Moreover, the inferred values compared very well with independent observations by collocated cloud sensing systems. We then generalized the diffusion model to account for absorption and explored the possibility of probing dense plumes of absorbing aerosol (e.g., smoke, dust, ash) near their sources—a topic a considerable interest to several scientific communities. Due to the dominance of absorption, we only anticipate the possibility of obtaining the particulates' single scattering albedo using, however, non-calibrated multiple-scattering lidar signals and constraining the relationship between the plume's optical and geometrical thicknesses.

Turning from atmospheric to surface-level media, we echoed the optimism of Várnai and Cahalan about the application of modified multiple scattering cloud lidar systems for probing sea ice and clean snow. We also extended their exploration into the realm of dirty (polluted) snow, which may be partly why the arctic regions are experiencing such rapid climate change. We concluded that, as long as we have ancillary information about the scattering properties of the snow, we can infer its single scattering albedo without the need for accurate radiometric calibration that plagues passive instruments.

Finally, we examined the possibility of using a down-looking multiple scattering lidar to perform a bathymetry of highly turbid coastal waters, a situation where direct detection of the underlaying surface signal is inhibited. We concluded that such an extension of standard laser bathymetry to situations where the water is optically thick enough to hide this direct return in multiply scattered laser light is possible as long as the instrumentation is available to measure off-beam this highly scattered laser light in highly stretched pulses. This last potential application of multiple scattering lidar is definitely worth pursuing with a more detailed feasibility study.

ACKNOWLEDGMENTS

The research was carried out at the Jet Propulsion Laboratory, California Institute of Technology, under a contract with the National Aeronautics and Space Administration. I am grateful for sustained financial support from NASA's Radiation Sciences Program managed by Drs. Hal Maring and Lucia Tsaoussi. The DOE/ARM Program funded the cloud remote sensing part of the multiple scattering lidar project. I thank Bob Cahalan, Támas Várnai and Matt McGill (GSFC), as well as Nicola Pounder and Robin Hogan (U. of Reading), for many exciting discussions about THOR, Steve Love (LANL) and Igor Polonsky (CSU) about WAIL, Dave Winker (LaRC) about LITE, Luc Bissonnette and Gilles Roy (DRDC) about MFOV, Frank Evans (U. of Colorado) and Paul Lawson (SPEC) about in situ cloud lidar, and many others that have shown an interest in multiple scattering lidar over the years. Special thanks go to Warren Wiscombe for his early and unwavering support, to Sasha Marshak for help with the early numerical and analytical modeling of cloud Green functions (during our glorious "radiative smoothing" period), to Craig Bohren for spirited early debates, and to the deeply regretted Jim Weinman, once again for being a pioneer.

REFERENCES

[1] Mishchenko, M. I., "Vector radiative transfer equation for arbitrarily shaped and arbitrarily oriented particles: A microphysical derivation from statistical electromagnetics," *Appl. Opt.* **41**, 7114–7135 (2002).

[2] Ganapol, B. D., Kornreich, D. E., Dahl, J. A., Nigg, D. W., Jahshan, S. N., and Temple, C. A., "The searchlight problem for neutrons in a semi-infinite medium," *Nucl. Sci. Eng.* **118**, 38–53 (1994).

[3] Kornreich, D. E. and Ganapol, B. D., "Numerical evaluation of the three-dimensional searchlight problem in a half-space," *Nucl. Sci. Eng.* **127**, 317–337 (1997).

[4] Machida, M., Panasyuk, G. Y., Schotland, J. C., and Markel, V. A., "The Green's function for the radiative transport equation in the slab geometry," *Journal of Physics A: Mathematical and Theoretical* **43**(6), 065402 (2010).

[5] Machida, M., Panasyuk, G. Y., Schotland, J. C., and Markel, V. A., "Corrigendum: The Green's function for the radiative transport equation in the slab geometry," *Journal of Physics A: Mathematical and Theoretical* **45**(45), 459501 (2012).

[6] Evans, K. F., "The spherical harmonics discrete ordinate method for three-dimensional atmospheric radiative transfer," *J. Atmos. Sci.* **55**, 429–446 (1998).

[7] Deirmendjian, D., [*Electromagnetic Scattering on Spherical Polydispersions*], Elsevier, New York, NY (1969).

[8] Bohren, C. F. and Huffman, D. R., [*Absorption and Scattering of Light by Small Particles*], Wiley, New York, NY (1983).

[9] Winker, D. M., Couch, R. H., and McCormick, M. P., "An overview of LITE: NASA's Lidar In-space Technology Experiment," *Proc. IEEE* **84**, 164–180 (1996).

[10] Polonsky, I. N., Love, S. P., and Davis, A. B., "Wide-Angle Imaging Lidar deployment at the ARM Southern Great Plains site: Intercomparison of cloud property retrievals," *J. Atmos. Ocean. Tech.* **22**, 628–648 (2005).

[11] Cahalan, R. F., McGill, M. J., Kolasinski, J., Várnai, T., and Yetzer, K., "THOR, cloud THickness from Offbeam lidar Returns," *J. Atmos. Ocean. Tech.* **22**, 605–627 (2005).

[12] Roy, G., Bissonnette, L. R., Bastille, C., Valle, G., et al., "Estimation of cloud droplet size density distribution from multiple-field-of-view lidar returns," *Optical Engineering* **36**(12), 3404–3415 (1997).

[13] Bissonnette, L. R., Roy, G., and Roy, N., "Multiple-scattering-based lidar retrieval: Method and results of cloud probings," *Appl. Opt.* **44**(26), 5565–5581 (2005).

[14] Klett, J. D., "Stable analytical inversion solution for processing lidar returns," *Appl. Opt.* **20**(2), 211–220 (1981).

[15] Platt, C. M. R., "Remote sounding of high clouds. III: Monte Carlo calculations of multiple-scattered lidar returns," *J. Atmos. Sci.* **38**(1), 156–167 (1981).

[16] Bissonnette, L. R., Bruscaglioni, P., Ismaelli, A., Zaccanti, G., Cohen, A., Benayahu, Y., Kleiman, M., Egert, S., Flesia, C., Schwendimann, P., et al., "Lidar multiple scattering from clouds," *Applied Physics B* **60**(4), 355–362 (1995).

[17] Zege, E. P., Katsev, I. L., and Polonsky, I. N., "Analytical solution to LIDAR return signals from clouds with regard to multiple scattering," *Applied Physics B* **60**(4), 345–353 (1995).

[18] Irvine, W. M., "The formation of absorption bands and the distribution of photon optical paths in a scattering atmosphere," *Bull. Astron. Inst. Neth.* **17**, 226–279 (1964).

[19] Ivanov, V. V. and Sabashvili, S. A., "Transfer of resonance radiation and photon random walks," *Astrophysics and Space Science* **17**, 13–22 (1972).

[20] Min, Q. and Harrison, L., "Joint statistics of photon path length and cloud optical depth," *Geophys. Res. Lett.* **26**, 1425–1428 (1999).

[21] Davis, A. B., Polonsky, I. N., and Marshak, A., "Space-time Green functions for diffusive radiation transport, in application to active and passive cloud probing," in [*Light Scattering Reviews*], Kokhanovsky, A. A., ed., **4**, 169–292, Springer-Praxis, Heidelberg, Germany (2009).

[22] Love, S. P., Davis, A. B., Rohde, C. A., Tellier, L., and Ho, C., "Active probing of cloud multiple scattering, optical depth, vertical thickness, and liquid water content using Wide-Angle Imaging Lidar," in [*Atmospheric Radiation Measurements and Applications in Climate*], Shaw, J. A., ed., *Proc. SPIE* **4815**, 129–138 (2002).

[23] King, M. D., Radke, L. F., and Hobbs, P. V., "Determination of the spectral absorption of solar radiation by marine stratocumulus clouds from airborne measurements within clouds," *J. Atmos. Sci.* **47**, 894–907 (1990).
[24] Gatebe, C. K., Várnai, T., Poudyal, R., Ichoku, C., and King, M. D., "Taking the pulse of pyrocumulus clouds," *Atmospheric Environment* **52**, 121–130 (2012).
[25] Case, K. M. and Zweifel, P. F., [*Linear Transport Theory*], Addison-Wesley, Reading, Ma (1967).
[26] Meador, W. E. and Weaver, W. R., "Two-stream approximations to radiative transfer in planetary atmospheres: A unified description of existing methods and a new improvement," *J. Atmos. Sci.* **37**, 630–643 (1980).
[27] Joseph, J. H., Wiscombe, W. J., and Weinman, J. A., "The delta-Eddington approximation for radiative flux transfer," *J. Atmos. Sci.* **33**, 2452–2459 (1976).
[28] Polonsky, I. N. and Davis, A. B., "Lateral photon transport in dense scattering and weakly absorbing media of finite thickness: Asymtotic analysis of the space-time Green function," *J. Opt. Soc. Am. A* **21**, 1018–1025 (2004).
[29] Hogan, R. J. and Battaglia, A., "Fast lidar and radar multiple-scattering models, Part 2: Wide-angle scattering using the time-dependent two-stream approximation," *J. Atmos. Sci.* **65**, 3636–3651 (2008).
[30] Pounder, N. L., Hogan, R. J., Várnai, T., Battaglia, A., and Cahalan, R. F., "A variational method to retrieve the extinction profile in liquid clouds using multiple-field-of-view lidar," *Journal of Applied Meteorology and Climatology* **51**(2), 350–365 (2012).
[31] Schutz, B. E., Zwally, H. J., Shuman, C. A., Hancock, D., and DiMarzio, J. P., "Overview of the ICESat mission," *Geophys. Res. Lett.* **32**(21), L21S01 (2005).
[32] Winker, D. M., Vaughan, M. A., Omar, A., Hu, Y., Powell, K. A., Liu, Z., Hunt, W. H., and Young, S. A., "Overview of the CALIPSO mission and CALIOP data processing algorithms," *Journal of Atmospheric and Oceanic Technology* **26**(11), 2310–2323 (2009).
[33] Davis, A. B., "Multiple-scattering lidar from both sides of the clouds: Addressing internal structure," *J. Geophys. Res.* **D113**, 14S10, doi:10.1029/2007JD009666 (2008).
[34] Evans, K. F., Lawson, R. P., Zmarzly, P., and O'Connor, D., "In situ cloud sensing with multiple scattering cloud lidar: Simulations and demonstration," *J. Atmos. Ocean. Tech.* **20**, 1505–1522 (2003).
[35] Evans, K. F., O'Connor, D., Zmarzly, P., and Lawson, R. P., "In situ cloud sensing with multiple scattering cloud lidar: Design and validation of an airborne sensor," *J. Atmos. Ocean. Tech.* **23**, 1068–1081 (2006).
[36] Davis, A. B., Cahalan, R. F., Spinhirne, J. D., M.J, M., and Love, S. P., "Off-beam lidar: An emerging technique in cloud remote sensing based on radiative Green-function theory in the diffusion domain," *Phys. Chem. Earth* **B24**, 177–185 [Erratum 757–765] (1999).
[37] Schuster, A., "Radiation through a foggy atmosphere," *Astrophys. J.* **21**, 1–22 (1905).
[38] Mishchenko, M. I. and Travis, L. D., "Satellite retrieval of aerosol properties over the ocean using polarization as well as intensity of reflected sunlight," *J. Geophys. Res.* **102**(D14), 16989–17 (1997).
[39] Herman, M., Deuzé, J. L., Devaux, C., Goloub, P., Bréon, F.-M., and Tanré, D., "Remote sensing of aerosols over land surfaces including polarization measurements and application to POLDER measurements," *J. Geophys. Res.* **102**(D14), 17039–17049 (1997).
[40] Várnai, T. and Cahalan, R. F., "Potential for airborne offbeam lidar measurements of snow and sea ice thickness," *J. Geophys. Res.* **C112**, 12S90, doi:10.1029/2007JC004091 (2007).
[41] Várnai, T. and Cahalan, R. F., "Modeling and analysis of offbeam lidar returns from thick clouds, snow, and sea ice," in [*International Conference on Mathematics, Computational Methods and Reactor Physics, Saratoga Springs, NY*], American Nuclear Society (2009).
[42] Warren, S. G., "Optical properties of snow," *Reviews of Geophysics* **20**(1), 67–89 (1982).
[43] Hudak, A. T., Evans, J. S., and Stuart Smith, A. M., "LiDAR utility for natural resource managers," *Remote Sensing* **1**(4), 934–951 (2009).
[44] Hopkinson, C., Sitar, M., Chasmer, L., and Treitz, P., "Mapping snowpack depth beneath forest canopies using airborne lidar," *Photogrammetric engineering and remote sensing* **70**(3), 323–330 (2004).
[45] Steinvall, O., Klevebrant, H., Lexander, J., and Widen, A., "Laser depth sounding in the Baltic Sea," *Appl. Opt.* **20**(19), 3284–3286 (1981).